Research Square

Preprints are preliminary reports that have not undergone peer review.
They should not be considered conclusive, used to inform clinical practice,
or referenced by the media as validated information.

FAM193A inhibits bladder cancer cell invasion and migration via PHD3/NF-κB pathway

Kuangzheng Liu
Ulm University Hospital
Junnan Liu
Ulm University Hospital
Xue Wang
Ulm University Hospital
Wencheng Jiang
Ulm University Hospital
Hengchuan Liu
Ulm University Hospital
Xiangyu Zhang
Ulm University Hospital
Zhiyu Wang
Ulm University Hospital
Gregoire Najjar
Ulm University Hospital
Anca Azoitei
Ulm University Hospital
Christian Bolenz
Ulm University Hospital
Cagatay Günes
Cagatay.Guenes@uni-ulm.de
Ulm University Hospital

Research Article

Keywords: Bladder cancer, MIBC, NMIBC, invasion, metastasis, RNAi Screening

Posted Date: November 19th, 2026

DOI: https://doi.org/10.21203/rs.3.rs-11612345/v1

License: This work is licensed under a Creative Commons Attribution 4.0 International License.
Read Full License

Additional Declarations: No competing interests reported.

FAM193A inhibits bladder cancer cell invasion and migration via PHD3/NF-κB pathway

Kuangzheng Liu[1], Junnan Liu[1, #], Xue Wang[1, &], Wencheng Jiang[1, §], Hengchuan Liu[1], Xiangyu Zhang[1], Zhiyu Wang[1], Gregoire Najjar[1], Anca Azoitei[1], Christian Bolenz[1] and Cagatay Günes[1,*]

[1] Department of Urology, Ulm University Hospital, Ulm, Germany

[#] Current Address: Department of Urology, Mayo Clinic College of Medicine and Science, Rochester, MN, USA

[&] Current Address: Mol. Pharmacology and Exp. Therapeutics, Mayo Clinic, Rochester, MN, USA

[§] Current Address: Department of Molecular Pharmacology and Therapeutics, Columbia University Irving Medical Center, New York, NY, USA

*Corresponding author. Prof. Dr. Cagatay Günes
E-mail: Cagatay.Guenes@uni-ulm.de
Phone: +49-731-500 58019

Abstract

Despite recent advances in molecular profiling that have revealed several cellular pathways involved in muscle-invasive bladder cancer progression, the underlying mechanisms of invasion remain elusive. Here, using a functional RNA interference screen, we identify *FAM193A* (Family with sequence similarity 193 member A) as a suppressor of BC cell migration and invasion. *FAM193A* expression is reduced in invasive BC cell lines, primary bladder tumours and muscle-invasive disease, and low expression is associated with adverse patient outcomes. We show that depletion of *FAM193A* enhances migration and invasion and impairs cell-cell adhesion, whereas ectopic expression suppresses cell motility and promotes intercellular cohesion without substantially affecting cell viability. Mechanistically, FAM193A associates with the nuclear factor-κB (NF-κB) subunit P65 and prolyl hydroxylase domain protein 3 (PHD3), stabilizes PHD3 and modulates stimulus-dependent PHD3-P65 complex assembly. Importantly, FAM193A preferentially associates with non-phosphorylated P65 and impairs sustained P65 Ser536 phosphorylation, thereby attenuating NF-κB transcriptional activity and the expression of selected NF-κB-responsive genes. Consistent with the established roles of TNFα/NF-κB and PHD3 in tumour-cell migration and invasion in several malignancies, FAM193A regulates cell migration and invasion by modulating PHD3-P65/NF-κB pathway in BC cell lines. These findings identify FAM193A as a stress-responsive regulator that links PHD3 to the termination of pro-invasive NF-κB signalling in BC.

Key words: *Bladder cancer · MIBC · NMIBC · bninvasion · metastasis · RNAi Screening*

Background

Bladder cancer (BC) is among the most common cancers worldwide and a significant global health burden [1]. It encompasses two clinically distinct types: non-muscle-invasive BC (NMIBC) and muscle-invasive BC (MIBC). NMIBC accounts for approximately 70% to 75% of newly diagnosed cases and has a high disease-specific 5-year survival rate exceeding 90% [2, 3]. In contrast, MIBC has a significantly poorer prognosis, with a 5-year overall survival rate of approximately 50% of patients with local invasion of cancer cells into muscle tissue, while survival rates drop to ~10% with further invasive and metastatic progression of the tumours [4]. Genomic and transcriptomic studies have further resolved BC into molecularly heterogeneous subtypes with differing differentiation states, immune contexts and therapeutic vulnerabilities [5-7]. Despite the recent advances, the molecular events that permit urothelial tumour cells to transition from a relatively cohesive, low-invasive state to a migratory and invasive phenotype remain incompletely understood. Given the substantial disparity in clinical outcomes between NMIBC and MIBC, understanding the molecular mechanisms underlying BC invasion and metastasis is particularly crucial.

Here, we employed a functional RNA interference screening in combination with the Boyden chamber cell invasion assay in low-invasive RT4 BC cell line to identify genes whose depletion promotes early invasive behaviour. A total of 19 candidate genes were identified from the screening as potential regulators of BC cell invasion. Among these genes, *FAM193A* (Family with sequence similarity 193 member A) attracted particular interest, as its loss markedly enhanced BC cell invasion, while its role in BC progression remains largely unexplored. *FAM193A*, also known as C4orf8 (Chromosome 4 open reading frame 8), is encoded by the *FAM193A* gene. Genes classified as “family with sequence similarity” exhibit conserved sequences, whereas the functions of their encoded proteins remain largely unknown [8]. To date, FAM193A is a poorly characterised protein for which little cancer-specific information is available. A recent study identified FAM193A as a positive regulator of p53 signalling through interaction with MDM4, suggesting that FAM193A may participate in stress-responsive tumour-

suppressive networks [9]. Loss of FAM193A impaired p53-dependent transcriptional responses and reduced cellular sensitivity to MDM2/MDM4 inhibition. These findings establish FAM193A as a crucial component of p53-mediated tumour suppressive signalling and suggest its potential relevance in cancer biology. However, its regulation at the protein level, its subcellular behaviour and its possible contribution to invasion have not been established.

In the present study, biochemical and cell biology experiments identified a novel network of FAM193A, Prolyl hydroxylase domain protein 3 (PHD3; encoded by *EGLN3*) and the nuclear factor-κB (NF-κB) pathway in the regulation of cell migration and invasion.

The canonical NF-κB pathway is typically initiated by inflammatory cues such as tumour necrosis factor alpha (TNFα), which activate the IκB kinase (IKK) complex, induce IκB degradation and permit RELA/P65-containing NF-κB dimers to accumulate in the nucleus [10, 11]. NF-κB output is nevertheless shaped by additional regulatory layers, including phosphorylation of P65, assembly of protein complexes, chromatin engagement and pathway-termination mechanisms [12]. Ser536 phosphorylation of P65 is frequently associated with enhanced transcriptional competence, although its functional consequences depend on stimulus and cellular context [13]. Persistent or incompletely terminated NF-κB activity can sustain inflammatory transcriptional programmes that favour tumour progression. Activation of NF-κB has been linked to proliferation, survival, epithelial plasticity, migration and invasion [14-17]. Importantly, several observations support a functional contribution of NF-κB to urothelial cancer aggressiveness: increased P65 activity promotes migration and invasion in BC models, in part through regulation of Rho-family signalling and matrix-remodelling programmes [18, 19]; urothelial tumourigenesis can also be reinforced by reciprocal signalling between NF-κB and the androgen receptor [20], while inflammatory cytokines stimulate BC motility through NF-κB-dependent transcription [21]. These studies establish NF-κB as a plausible driver of invasive behaviour, but they also highlight an unresolved question: which endogenous factors restrain the duration and amplitude of NF-κB signalling in BC cells?

Prolyl hydroxylase domain protein 3 (PHD3; encoded by *EGLN3*) is best known as an oxygen-sensitive enzyme that contributes to the regulation of hypoxia-inducible factors [22]. PHD proteins also participate in oxygen-independent signalling and have been reported to interact with components of the NF-κB pathway. Depending on cell type and stimulus, PHD3 can modulate IKK activity, associate with P65 or alter inflammatory transcription [23-25]. PHD3 has additionally been implicated in cancer-cell adhesion and metastasis, although its effects appear context dependent [26, 27]. For instance, PHD3 has been shown to inhibit metastasis in colon cancer cells via the occludin–p38 pathway and to restrain glioblastoma progression through regulated protein stability [26, 27]. PHD3 has been reported to participate in the regulation of NF-κB signalling; however, its precise role remains controversial. On the one hand, PHD3 has been reported to physically interact with NF-κB/P65 and function as a co-activator in response to TNFα; on the other hand, other studies indicate that PHD3 suppresses NF-κB activation by suppressing IKKβ activity [23, 25, 28]. These data suggest that PHD3 can act as a tumour suppressor or may promote tumour progression in a context dependent manner.

Our findings indicate that FAM193A suppresses BC invasion and migration through coordinated regulation of the NF-κB/PHD3 signalling axis. Overall, our results identify FAM193A as a stress-inducible regulator that restrains bladder cancer cell migration and invasion. In unstressed cells, FAM193A is kept at low levels through proteasome-dependent turnover, whereas genotoxic stress or TNFα exposure promotes its accumulation. Mechanistically, FAM193A interacts with both PHD3 and P65, stabilising PHD3 while altering the composition and/or activity of P65-containing complexes. These effects attenuate prolonged phosphorylation of P65 at Ser536, dampen a subset of NF-κB-dependent transcriptional responses, and reduce TNFα-induced invasive behaviour. Together, these findings position FAM193A at the interface of proteostatic regulation and inflammatory signalling, where it acts to constrain persistent NF-κB activity and thereby limit urothelial cancer invasion.

Materials and Methods

Cell lines

HEK293T and HeLa cells were cultured in DMEM (Cat. No. 41965-039, Gibco, Thermo Fisher Scientific, Waltham, MA, USA), supplemented with 10% fetal calf serum (FCS; Cat. No. AC-SM-0190, Sigma-Aldrich, St. Louis, MO, USA) and 1% penicillin/streptomycin (P/S; Cat. No. P06-07100, PAN Biotech, Aidenbach, Germany). Y235T cells were a gift from Prof. Jennifer Southgate (University College London, UK). HBLAK cells were a gift from Michele Hoffmann (Department of Urology, Düsseldorf, Germany). Y235T and HBLAK cells were cultured in complete epithelial culture medium, CnT-Prime (Cat. No. CnT-PR, CELLnTEC, Bern, Switzerland). RT4, RT112, T24 and UMUC3 cells were cultured in RPMI-1640 medium (Cat. No. 21875-034, Gibco, Thermo Fisher Scientific, Waltham, MA, USA) supplemented with 10% FCS and 1% P/S. BFTC-905 cells were cultured in DMEM supplemented with 20% FCS and 1% P/S. BC61 cells were cultured in DMEM/F-12 medium supplemented with 10% FCS and 1% P/S. All cell lines were maintained at 37 °C in a humidified atmosphere with 5% carbon dioxide.

shRNA Library and RNAi Screen

The shRNA library has been described previously [29]. RT4 cells were infected with a pooled lentiviral shRNA library targeting 16.500 human genes (pGIPZ-based library), at a multiplicity of infection (MOI) of 0.3 to ensure single integration per cell. Infected cells were selected with puromycin (2 µg mL^{-1}) for 7 days. Following puromycin selection, (1×10^5) cells were seeded into the upper chamber of each 24-well Boyden (8 µm pore size, Cat. No. 354480, Corning, NY 14831, USA) coated with Matrigel Basement Membrane Matrix (0.25 µg/µl, Cat. No. 354234, Corning, NY 14831, USA). In total, $2.4x10^7$ cells were seeded in ten 24-well plates, comprising 240 Boyden chambers. In addition, one 24-well Boyden chamber was seeded with RT4-shScr or RT4-shLuc as control shRNAs (12 Boyden chamber setups each). After 48 h, cells that had migrated through the membrane and grew in the culture-well were collected, expanded, and subjected to two additional rounds of selection using the same Boyden

chamber procedure. Following the final screening round, genomic DNA was prepared and the integrated shRNA sequences that promote cell invasion were identified by PCR amplification, followed by Sanger sequencing.

Plasmids, single shRNAs, and sgRNA Constructs

V5-tagged FAM193A expression plasmid was obtained from the DNASU Plasmid Repository (Arizona State University, Tempe, AZ, USA). PHD3 expression plasmid was obtained from Addgene (plasmid #79115). Although annotated as containing a C-terminal V5 tag, sequence analysis revealed that the V5 coding sequence is not translated, which was further confirmed by immunoblotting. Halo-tagged full-length FAM193A and FAM193A truncation constructs were generously provided by Dr. Zdenek Andrysik (Department of Pharmacology, University of Colorado Anschutz Medical Campus, Aurora, CO, USA).

Lentiviral shRNA vectors encoding FAM193A/EGLN3/RELA-targeting shRNAs, as well as the non-targeting control shRNAs (sh-Luc and sh-Scr), were obtained from the MISSION shRNA library (Sigma-Aldrich, St. Louis, MO, USA). For CRISPR–Cas9 mediated gene knockout, candidate sgRNAs targeting FAM193A/SQSTM1 were identified from the Human GeCKO v2 library. The predicted on-target activities of sgRNAs were further evaluated using the CRISPR Design Tool developed by the laboratory of Feng Zhang. The three highest-scoring sgRNAs were selected and cloned into the pLentiCRISPR v2 vector (Addgene plasmid #52961). Detailed information on all plasmids, shRNAs, and sgRNAs used in this study is provided in Supplementary Table ST2.

DNA transfection, viral production, and generation of stable cell lines

Plasmid transfection was performed using polyethyleneimine (PEI; Cat. No. 23966, Polysciences, Warrington, PA, USA) or Lipofectamine 3000 (Cat. No. L3000008, Thermo Fisher Scientific, Waltham, MA, USA) according to the manufacturers' instructions. Stable cell lines generated by plasmid transfection were established by antibiotic selection using Geneticin (Cat. No. 4727878001, G418 sulfate; 600 μg mL^{-1}, Roche, Rotkreuz, Switzerland),

puromycin (Cat. No. A11138-03, 2 µg mL^{-1}, Thermo Fisher Scientific, Waltham, MA, USA), or blasticidin (Cat. No. A111-3903, 12.5 µg mL^{-1}, Thermo Fisher Scientific, Waltham, MA, USA), as appropriate. For virus production, HEK293T cells at 60–70% confluency were transfected with the indicated plasmids. For lentiviral vector production, 30 µl PEI, 1.8 µg psPAX2, 0.3 µg pMD2.G, and 5 µg transfer plasmid were mixed with 500 µl serum-free DMEM. For retroviral vector production, 30 µl PEI, 1.8 µg pCMV-Gag-Pol, 0.3 µg pCMV-VSV-G, and 5 µg transfer plasmid were mixed with 500 µl serum-free DMEM. Virus collection and cell infection were performed according to standard procedures. Virus-infected stable cell lines were established by antibiotic selection using puromycin (2 µg mL^{-1}) or blasticidin (12.5 µg mL^{-1}), as appropriate.

Drug and hypoxia treatments

Cells were treated with the indicated compounds under the experimental conditions described in the corresponding figure legends. Tumor necrosis factor alpha (TNFα; Cat. No. 300-01A, PeproTech, Cranbury, NJ, USA) was typically used at final concentrations of 10–20 ng mL^{-1}, while concentration-dependent experiments employed a range of 5–60 ng mL^{-1}, as specified in the corresponding figure legends. Epidermal growth factor (EGF; Cat. No. AF-100-15, PeproTech, Cranbury, NJ, USA) was used at a final concentration of 10 ng mL^{-1}. Doxorubicin hydrochloride (Dox; Cat. No. HY-15142, MedChemExpress, Monmouth Junction, NJ, USA) was used at a final concentration of 1 µM. MG132 (Cat. No. 474790, Sigma-Aldrich, St. Louis, MO, USA) was used at 5 µM for proteasome inhibition, actinomycin D (ActD; Cat. No. A9415, Sigma-Aldrich, St. Louis, MO, USA) at 2 µg mL^{-1} for transcriptional inhibition, and hydrogen peroxide (H_2O_2; Cat. No. H1009, Sigma-Aldrich, St. Louis, MO, USA) at 100 µM /1 mM to induce oxidative stress. Hypoxic conditions, indicated as 1% O_2 in the figures, were generated using the AnaeroGen™ A mini system (Cat. No. 1.32369.0001, Merck, Darmstadt, Germany) according to the manufacturer's instructions for the indicated durations. Establishment of the low-oxygen atmosphere was verified using the Anaerotest® indicator strip (Cat. No. 1.32371.0001, Merck, Darmstadt, Germany).

Antibodies

A list of antibodies used in this study is provided in Supplementary Table ST3.

Protein extraction and Western blot (Immunoblot)

For protein expression analysis, 5 × 10^5 cells were seeded in a 10 cm culture dish and harvested when cell confluence reached 70%–80%. Cells were lysed using RIPA lysis buffer (Cat. No. R2078-50ML, Sigma-Aldrich, St. Louis, MO, USA) supplemented with protease inhibitors (Cat. No. 0469311601, Roche, Rotkreuz, Switzerland) and phosphatase inhibitors (Cat. No. 04906837001, Roche, Rotkreuz, Switzerland). Lysates were incubated by rotation at 4 °C for 40 minutes, followed by centrifugation at 16,000 × g for 16 minutes. Protein concentration was determined using the bicinchoninic acid (BCA) method (Cat. No. 71285-M, Sigma-Aldrich, St. Louis, MO, USA). Equal amounts of protein (10–40 µg) were separated by SDS–PAGE and analysed by immunoblotting using the specified antibody.

Ex vivo porcine bladder invasion model

Porcine bladders were obtained from a local abattoir immediately after slaughter. Ex vivo invasion assay was primarily conducted according to the method previously described by Wezel et al. [30]. Using a Zeiss Axio Imager.M2 microscope (Carl Zeiss Microscopy GmbH, Jena, Germany) equipped with a 20× objective, images were acquired from five randomly selected regions in each bladder tissue sample. Using ZEN software, cell invasion was quantitatively analysed by measuring the distance between the deepest invading cell and the seeding tissue surface. The experiment analysed the top 30 RT4, T24, or BFTC-905 cells with the strongest invasive capacity and calculated the average invasion depth.

Wound healing and Boyden chamber assays

Cell migration and invasion were assessed using wound healing and Boyden chamber assays as described previously [31]. Images were acquired using a Zeiss Axio Imager.M2 microscope (Carl Zeiss Microscopy GmbH, Jena, Germany) equipped with a 5× objective for wound healing assays and a 10× objective for Boyden chamber assays. For quantification, five different vision fields from each single repeat experiments were calculated for mean value.

Hanging drop assays

Cell aggregation was assessed using a hanging drop assay. Cells were resuspended in complete culture medium at a density of 1 × 10^5 cells/mL. Ten-microlitre drops of the cell suspension were placed on the inner surface of the lid of a 10-cm culture dish. The lid was then carefully inverted and placed over the culture dish containing 10 mL PBS to maintain humidity. Cells were incubated overnight at 37 °C in a humidified incubator. On the following day, the hanging drops were imaged to assess cell aggregation.

MTT assay

Cell viability was assessed using the MTT assay. RT4/T24/BFTC-905 cells were seeded in 96-well plates at densities of 1,000/500/500 cells per well, respectively, with six technical replicates per condition. At the indicated time points, cells were incubated with MTT reagent for 4 h. Formazan crystals were dissolved using a lysis solution containing DMSO, SDS and acetic acid, and absorbance was measured at 570 nm using a microplate reader.

RNA extraction, reverse transcription, and quantitative real-time PCR (RT–qPCR)

Total RNA was extracted using the RNeasy Mini Kit (Cat. No. 74106, Qiagen, Hilden, Germany) according to the manufacturer's instructions. Briefly, cells were washed with PBS and lysed in RLT buffer supplemented with 1% β-mercapto-ethanol (Cat. No. M6250-100ML, Sigma-Aldrich, St. Louis, MO, USA). RNA concentration and purity were determined by measuring absorbance at 260 and 280 nm using an Epoch microplate spectrophotometer (Biotek Instruments, Winooski, VT, USA). For cDNA synthesis, 100 ng of total RNA was reverse transcribed using the GoScript Reverse Transcription System (Cat. No. A5001, Promega, Madison, WI, USA). Quantitative real-time PCR (RT–qPCR) was performed using a QuantStudio 3 Real-Time PCR System (Applied Biosystems, Foster City, CA, USA) with SYBR Green-based detection chemistry. Each reaction contained diluted cDNA template and gene-specific primers listed in Supplementary Tables ST4. Relative mRNA expression levels were calculated using the (2^-ΔCt ×100) method by normalizing to GAPDH expression.

Genomic DNA isolation

Genomic DNA was isolated from cultured cells using the QIAamp DNA Mini Kit (Cat. No. 51304, Qiagen, Hilden, Germany) according to the manufacturer's instructions. Target genomic regions or integrated shRNA sequences were subsequently amplified by PCR and analysed by Sanger sequencing. PCR and sequencing primers are listed in Supplementary Table ST5.

Immunofluorescence (IF) and proximity ligation assay (PLA)

Cells were seeded onto 19-mm glass coverslips placed in 12-well plates and cultured for at least 48 h before staining. For immunofluorescence staining, cells were washed once with PBS, fixed with 4% paraformaldehyde (PFA, Cat. No. 20909.290, VWR, Darmstadt, Germany) for 10 min at room temperature, and permeabilized with 1% Triton X-100 (Cat. No. T8787-250ML, Sigma-Aldrich, St. Louis, MO, USA) in PBS. After three washes with PBS, cells were blocked in PBS containing 1% bovine serum albumin (BSA) for 1 h at room temperature. Samples were then incubated overnight at 4 °C with primary antibodies diluted in PBS containing 1% BSA. The following day, coverslips were washed three times with PBST (PBS containing 0.5% Tween-20) and incubated with the appropriate fluorophore-conjugated secondary antibodies. Nuclei were counterstained with DAPI and coverslips were mounted using ProLong Gold Antifade Mountant with DAPI (Cat. No. P36934, Thermo Fisher Scientific, Waltham, MA, USA).

For proximity ligation assay (PLA), cells grown on coverslips were fixed and permeabilized as described above. PLA was performed using the Duolink In Situ Orange Starter Kit (Cat. No. DUO92102, Sigma-Aldrich, St. Louis, MO, USA) according to the manufacturer’s instructions. After blocking, samples were incubated overnight at 4 °C with the indicated primary antibody pairs. The following day, coverslips were incubated with species-specific PLA probes, followed by ligation and amplification using the reagents provided in the kit. Nuclei were counterstained with DAPI, and coverslips were mounted using the mounting medium supplied with the kit. PLA signals were visualized as discrete fluorescent puncta.

Images were acquired using a Zeiss Axio Imager.M2 microscope (Carl Zeiss Microscopy GmbH, Jena, Germany) equipped with a 63× oil-immersion objective.

Immunohistochemistry (IHC)

Paraffin-embedded tissue sections (4 µm) were subjected to immunohistochemical staining according to standard protocols. Briefly, sections were deparaffinized, rehydrated, subjected to antigen retrieval with citrate buffer, and treated to block endogenous peroxidase activity. Slides were then incubated overnight at 4 °C with the indicated primary antibodies. After washing, sections were incubated with HRP-conjugated secondary antibodies and developed using 3,3′-diaminobenzidine (DAB, Cat. No. ACH500, ScyTek, Logan, UT, USA). Nuclei were counterstained with haematoxylin, and slides were dehydrated and mounted for microscopic analysis.

NF-κB dual-luciferase reporter assay

The 3×κB firefly luciferase reporter plasmid and Renilla luciferase control plasmid were generously provided by Dr. Alexey Ushmorov (Institute of Physiological Chemistry, Ulm University, Ulm, Germany). Cells were seeded in 12-well plates and transfected at approximately 70% confluency using Lipofectamine 3000. Expression plasmids were transfected as indicated in the corresponding figure legends. The 3×κB firefly luciferase reporter plasmid and Renilla luciferase control plasmid were co-transfected at a ratio of 30:1. Twenty-four hours after transfection, the culture medium was replaced and cells were subjected to the indicated treatments for the specified durations. At the indicated endpoint, cells were harvested and lysed using Passive Lysis Buffer. Firefly and Renilla luciferase activities were measured using the Dual-Luciferase Reporter Assay System (Cat. No. E1910, Promega, Madison, WI, USA) according to the manufacturer's instructions. NF-κB reporter activity was normalized to Renilla luciferase activity and expressed relative to the indicated control condition.

Co-immunoprecipitation (Co-IP) and sequential immunoprecipitation (Seq-IP)

Cells were lysed in ice-cold IP lysis buffer (25 mM Tris-HCl, 150 mM NaCl, 1 mM EDTA, 0.5% NP-40, and 5% glycerol, pH 7.6) supplemented with protease and phosphatase inhibitors. Following lysis for 40 min at 4 °C with rotation, lysates were clarified by centrifugation at 16,000 × g for 16 min at 4 °C. Protein concentrations were determined using the BCA Protein Assay Kit. Equal amounts of protein were incubated overnight at 4 °C with the indicated primary antibodies or the corresponding control IgG. Protein A (Cat. No. 20333, Thermo Fisher Scientific, Waltham, MA, USA) or Protein G agarose beads (Cat. No. 20398, Thermo Fisher Scientific, Waltham, MA, USA) were then added and incubated for an additional 4 h at 4 °C. Beads were washed five times with IP lysis buffer, and bound proteins were eluted by boiling in 2× SDS sample buffer supplemented with 100 mM DTT. Immunoprecipitated proteins and input lysates were analysed by SDS–PAGE and immunoblotting using the indicated antibodies.

For sequential immunoprecipitation, the first immunoprecipitation was performed as described above, except that bound proteins were eluted using Pierce IgG Elution Buffer (Cat. No. 21004, Thermo Fisher Scientific, Waltham, MA, USA) instead of SDS sample buffer. Beads were incubated with the elution buffer for 2 min, followed by centrifugation to collect the eluate, which was immediately neutralized with 1 M Tris (pH 9.0). The elution was repeated once, and the combined eluates were subjected to a second immunoprecipitation using the indicated antibody. The resulting immunoprecipitants were analysed by SDS–PAGE and immunoblotting.

Nuclear and cytoplasmic fractionation

Nuclear and cytoplasmic extracts were prepared using a modified buffer A/buffer C fractionation protocol. Briefly, cells were harvested, washed with ice-cold PBS, and resuspended in buffer A (10 mM HEPES, pH 7.9, 10 mM KCl, 0.1 mM EDTA, and 0.1 mM EGTA) supplemented with protease and phosphatase inhibitors. After incubation on ice for 15 min, NP-40 (Cat. No. ab142227, Abcam, Cambridge, UK) was added to a final concentration of either 0.25% or 0.5%, as indicated. Samples were vortexed for 5 s, incubated on ice for 1 min, vortexed again for 5 s, and centrifuged at either 16,000 × g for 2 min or 600 × g for 10 min. The resulting supernatant was collected as the cytoplasmic fraction. The nuclear pellet

was washed once with buffer A and subsequently extracted in buffer C (20 mM HEPES, pH 7.9, 400 mM NaCl, and 1 mM EDTA) supplemented with protease and phosphatase inhibitors for 30 min at 4 °C with rotation. Following centrifugation at 16,000 × g for 10 min, the supernatant was collected as the nuclear extract. Protein concentrations of cytoplasmic and nuclear fractions were determined using the BCA Protein Assay Kit and Bradford Protein Assay, respectively. Equal amounts of protein were analysed by SDS–PAGE and immunoblotting using the indicated antibodies.

Halo pulldown assay

Cells were lysed in ice-cold IP lysis buffer (25 mM Tris-HCl, 150 mM NaCl, 1 mM EDTA, 0.5% NP-40, and 5% glycerol, pH 7.6) supplemented with protease and phosphatase inhibitors. Following lysis for 40 min at 4 °C with rotation, lysates were clarified by centrifugation at 16,000 × g for 16 min at 4 °C. Protein concentrations were determined using the BCA Protein Assay Kit. HaloLink Resin (Cat. No. G1912, Promega, Madison, WI, USA) was pre-blocked with 5% BSA in IP lysis buffer for 1 h at room temperature and subsequently washed with IP lysis buffer. Equal amounts of protein lysate were then incubated with the resin for 2 h at 4 °C with rotation. After incubation, the resin was washed five times with IP lysis buffer to remove unbound proteins. Bound proteins were eluted by boiling in 2× SDS sample buffer supplemented with 100 mM DTT and analysed by SDS–PAGE and immunoblotting using the indicated antibodies.

BBN-induced BC mouse model

The BBN-induced BC mouse model was established as previously described [32]. Briefly, C57BL/6 mice received 0.1% N-butyl-N-(4-hydroxybutyl)-nitrosamine (BBN; Cat. No. B8061, Sigma-Aldrich, St. Louis, MO, USA) in the drinking water ad libitum for up to 8 months. Fresh BBN-containing drinking water was prepared weekly. Mice were sacrificed after 2, 4, 6, or 8 months of treatment, and bladder tissues were collected for histological analysis. All animal experiments were approved by the Baden-Württemberg Animal Ethics Committee (approval no. 35/9185.81-3/1326) and were performed in accordance with institutional guidelines.

Bioinformatics analysis

Genomic alteration frequencies of *FAM193A* across different cancer types were obtained directly from cBioPortal. Uniformly processed RNA-sequencing data from The Cancer Genome Atlas (TCGA) and the Genotype-Tissue Expression (GTEx) project were downloaded from the UCSC Xena database and analysed using R to compare *FAM193A* expression between BC and normal bladder tissues. The publicly available gene expression datasets GSE48075 and GSE32894 were obtained from the Gene Expression Omnibus (GEO) database and analysed using R. Correlations between *FAM193A* expression and the expression of NF-κB-related genes in the GSE32894 dataset were assessed using R and visualized as a bubble plot. TCGA BC survival analysis was performed using the Kaplan–Meier Plotter database. Survival data from GSE48075 were independently analysed in R, and survival curves were generated using the Kaplan–Meier method. Differences between survival curves were evaluated using the log-rank test. Protein–protein interaction datasets were obtained from the BioGRID database and used for interaction analyses and for Venn diagram generation; a list of the identified interacting proteins is provided in Supplementary Table ST6.

Single-cell transcriptomic analysis

Processed single-cell RNA-sequencing data from human bladder tumours were obtained from Juric et al. [33] (GEO accession GSE269877), comprising 27 tumour samples from 23 patients. Cell-type annotations were taken directly from the processed dataset provided by the original investigators, without de novo clustering or re-annotation. After exclusion of non-urothelial cells and cells designated as removed during sub-clustering, 183,320 urothelial cells were retained for downstream analysis.

Raw counts were aggregated across all retained urothelial cells within each tumour sample to generate pseudo-bulk expression profiles. Library-size normalization was performed using the trimmed mean of M values (TMM) method implemented in edgeR, and normalized log2 counts per million (logCPM) were used for downstream analyses. For patient-level inference, one

tumour sample was retained per patient, preferentially selecting a BCG-naïve sample when multiple longitudinal samples were available, resulting in 23 independent patient-level profiles.

Spearman correlations between FAM193A and six NF-κB-related genes examined in our bladder cancer cell experiments (*CXCL1, CXCL3, CXCL8, CXCL10, PTGS2,* and *IL1B*) were calculated across the 23 patient-level profiles, with Benjamini–Hochberg correction across the six genes. To account for potential differences between BCG-naïve and recurrent samples, additional linear models included sample status as a covariate.

For the selected six-gene *RELA*-positive target score, expression of each gene was standardized across the 23 patients and the standardized values were averaged for each patient. A broader *RELA*-positive target score was generated from QC-passed positively regulated *RELA* targets obtained from the CollecTRI/OmniPath transcription factor–target network [34] using the same gene-wise standardization and averaging procedure. Spearman correlations between *FAM193A* and each score were then calculated.

To determine whether the association between *FAM193A* and the six-gene score was stronger than expected from the broader *RELA*-positive target background, 10,000 random six-gene sets were sampled from the remaining *RELA*-positive target genes. Each random set was scored using the same procedure and correlated with *FAM193A* across the 23 patients. The one-sided empirical P value was calculated as the proportion of random-set correlations equal to or more negative than the observed six-gene correlation.

ChatGPT (OpenAI) was used to assist with drafting R code for the single-cell transcriptomic analyses described above. All analyses were executed, reviewed, and validated by the authors.

Statistical analysis

Statistical analyses of experimental data were performed using GraphPad Prism 10 (GraphPad Software, San Diego, CA, USA), whereas transcriptomic analyses were performed in R. Statistical tests are specified in the corresponding figure legends. Unless otherwise indicated, two-group experimental comparisons were performed using two-tailed Student's t-

tests, while multiple-group comparisons were performed using one-way or two-way ANOVA followed by appropriate multiple-comparisons tests. Non-parametric, correlation, survival, and regression analyses were performed as specified in the corresponding Methods sections and figure legends. $P < 0.05$ was considered statistically significant.

Experiment Repeats

All experiments presented in the main figures, including immunoprecipitations and immunoblots were performed at least in triplicates (n = 3 independent experiments), unless otherwise stated in the legends to the figures.

Results

FAM193A is downregulated in invasive BC and is associated with poor patient outcome

Matrigel-coated Boyden chamber assay is a simple, reliable, reproducible, and representative experimental approach for cancer cell invasion [35]. Please note that in the following we use the term 'Boyden chamber' for simplicity, although we always use Matrigel-coated Boyden chamber setups for the experiments presented here. In this study, we performed a pooled RNAi-screening with RT4 cells using a Boyden chamber-based selection strategy to identify genes and pathways regulating BC invasion (Fig. 1A). The RT4 cell line is characterized by non/low-invasive behaviour in a variety of cellular assays, including Boyden chamber and *ex vivo* model systems [30, 36]. Under the conditions described in the Materials and Methods section used in our laboratory, RT4 cells have very low invasive/transmigratory capacity in the Boyden chamber invasion assay. We observe earliest invasive parental RT4 cells 10 days after seeding the cells in Boyden chamber (Fig. S1A; Fig. S1B).

In order to assess how a specific gene KD would influence the invasive capacity of RT4 cells, we first used *ORP3* or *GJB3* knockdown (KD), based on our previous studies [37, 38]. In line with our earlier reports, invasive RT4 cells with *ORP3*-KD or *GJB3*-KD could be observed as early as 2 days post-seeding (Fig. S1C). Thus, we decided to conduct the RNAi-screening at the two-day time point. RT4 cells infected with a pooled shRNA library were seeded into Matrigel-coated Boyden chambers (see Materials and Methods section for detailed information on library composition, control shRNAs, as well as for cell and Boyden chamber numbers). Infected RT4 cells stably expressing shRNA plasmids were seeded into Matrigel-coated Boyden chamber setups. After 48 hours, cells that had invaded through the membrane and grew in the culture-well were collected, expanded, and subjected to two additional rounds of selection using the same Boyden chamber procedure to minimize potential false positives (Fig. 1A, left). Finally, RT4 cells carrying shRNAs that promote their invasive behaviour–were expanded and collected for downstream analyses.

The shRNA sequences in these cells were subsequently identified by genomic DNA extraction, PCR amplification, and sequencing (Fig. 1A, left). The screening identified 19 protein coding genes (Supplementary Table ST1). Subsequent *in silico* analyses (including TCGA gene expression and mutational data), initial mRNA expression data using a set of non/low invasive (HBLAK, Y235T, BC61, RT4) and invasive BC cell lines (T24, UMUC-3 and BFTC-905) identified three top candidate genes, i.e. *Vitamin D Receptor* (*VDR), Vestigial Like Family Member 1 (VGLL1)* and *Family with Sequence Similarity 193 Member A (FAM193A)* (Fig. 1A, right). As barely any information is available on FAM193A in BC, we decided to explore its role in migration and invasion of BC cells and to investigate potential pathways associated with FAM193A in this study. Please note, that the roles of VDR and VGLL1 proteins in BC are currently under investigation in separate studies in our laboratory.

FAM193A expression was relatively high in immortalized urothelial cells (HBLAK, Y235T) and low-invasive BC cell lines (BC61, RT4), compared to its expression in high-invasive BC cell lines (T24, UMUC-3 and BFTC-905) (Fig. 1B; both comparisons, $P < 0.0001$). This result supports a negative correlation between *FAM193A* expression levels and cellular invasive potential. Analysis of pan-cancer genomic datasets revealed that *FAM193A* mutations are particularly enriched in BC, along with UCEC (Uterine Corpus Endometrial Carcinoma) (about 6-8% of patients with mutations in *FAM193A*), compared with multiple other tumour types (Fig. 1C), suggesting a potential role for *FAM193A* dysregulation in bladder tumourigenesis. Consistently, our analysis of RNA-seq data from the TCGA-BLCA and GTEx cohorts revealed that *FAM193A* expression levels were significantly reduced in primary bladder tumours compared to normal bladder tissue (Wilcoxon test, $P < 0.001$; Fig. 1D) [5, 39, 40]. Furthermore, gene expression data of normal and tumour tissues using the BBN-induced mouse BC model revealed that *Fam193a* mRNA expression was significantly reduced in tumour tissues compared with control bladder tissues ($P = 0.0339$; Fig. S1D), consistent with the results obtained from human BC cohorts (Fig. 1D).

To further investigate the clinical relevance of *FAM193A* expression, we analysed its association with pathological characteristics in publicly available BC patient cohort GSE48075 that comprises 72 patients with muscle-invasive BC (MIBC) and 67 non-muscle-invasive BC (NMIBC, n=67) [41]. Notably, *FAM193A* expression was lower in the MIBC group compared to the NMIBC group (Wilcoxon test, P = 0.037; Fig. 1E). Given the association between *FAM193A* expression and aggressive disease characteristics, we subsequently evaluated its prognostic significance for patient survival. Kaplan–Meier survival analysis of the TCGA BC cohort (n = 404) demonstrated that patients with low *FAM193A* expression had significantly shorter overall survival (OS) than those with high *FAM193A* expression (log-rank P = 0.014; Fig. 1F). Similar associations were observed in the GSE48075 cohort, where low FAM193A expression was associated with poorer OS (log-rank P = 0.013; Fig. 1G) and disease-specific survival (log-rank P = 0.002; Fig. 1H).

In summary, these findings identify *FAM193A* as a potential suppressor of BC progression and reveal a significant association between its downregulation, aggressive tumour phenotypes, and poor clinical prognosis.

FAM193A suppresses migration and invasion of BC cells

In order to assess the accuracy of our initial screening results and to investigate the functional role of *FAM193A* in BC progression, we established loss-of-function and gain-of-function models in BC cell lines. As RT4 cells were used for the screening and based on its expression in BC cell lines (Fig. 1B) we chose RT4, T24 and BFTC-905 cells for these experiments. We find that shRNA-mediated gene knockdown effectively reduced *FAM193A* mRNA expression in RT4 cells (sh-*FAM193A*-1, P = 0.0219; sh-*FAM193A*-2, P = 0.0094; sh-*FAM193A*-3, P = 0.0077 versus sh-Luc). Unfortunately, endogenous protein levels could not be detected due to lack of suitable antibodies. For the ectopic expression, a V5-tagged FAM193A expression vector has been introduced in T24 or BFTC-905 cell lines showing significantly increased FAM193A mRNA and protein levels in T24 (P = 0.0005) and BFTC-905 (P = 0.0056) cells (Fig.

505 2A). Notably, although ectopic *FAM193A* expression significantly increased mRNA levels,
506 FAM193A protein levels remained low, likely due to low protein stability (see below).

507 MTT assays showed that altered FAM193A expression had no significant effect on the
508 viability/survival of BC cells (Fig. S2A). Next, we used the Boyden chamber invasion assay to
509 evaluate the effect of FAM193A on the invasive capacity of BC cells. Compared with the control
510 group (RT4-shLuc), silencing of *FAM193A* in RT4 cells significantly enhanced their invasive
511 capacity (One-way ANOVA, P = 0.0028). Conversely, ectopic expression of FAM193A
512 significantly inhibited the invasive capacity of T24 (P = 0.0004) and BFTC-905 (P = 0.0024)
513 cells (Fig. 2B), indicating that FAM193A negatively regulates the invasion of BC cells.

514 To determine whether FAM193A also affects cell migration, we performed wound-healing
515 assays, also referred to as scratch assays. Consistent with the results of the invasion assay,
516 FAM193A knockdown accelerated wound closure in RT4 cells (two-way ANOVA, column
517 factor, P = 0.0064), whereas FAM193A overexpression significantly delayed wound closure in
518 T24 (P = 0.0137) and BFTC-905 cells (P = 0.0011; Fig. 2C). These results indicate that
519 FAM193A suppresses the migration and invasion phenotypes of BC cells.

520 To further validate these observations using an independent genetic approach, we generated
521 RT4-p53DD-FAM193A knockout clones by CRISPR (Clustered Regularly Interspaced Short
522 Palindromic Repeats) technology, using three independent guide RNAs (gRNAs), along with
523 two independent control guide RNAs (gGFP). Please note that RT4 cells with a functionally
524 dead mutant p53, RT4-p53DD, was used for CRISPR-mediated gene knockout, based on our
525 earlier observations [36]. FAM193A knockout in RT4-p53DD was verified via Sanger
526 sequencing and ICE (Inference of CRISPR Edits) analysis (Fig. 2D; Fig. S2B).

527 To further investigate the role of FAM193A in BC cell invasion, we employed an *ex vivo* porcine
528 bladder invasion assay. Human RT4-p53DD and T24 cells were identified using human-
529 specific mitochondrial marker or an anti-HLA antibody, respectively. The impact of FAM193A
530 on cell invasion was quantified by measuring the distance of the 30 deepest invading cells from
531 the seeding surface into the bladder tissue, according to a quantification protocol previously

developed in our laboratory [37]. Consistent with their non/low-invasive phenotype, RT4-p53DD control cells showed no detectable invasion during the 28-day observation period, whereas RT4-p53DD-FAM193A-knockout cells invaded into the bladder tissue stroma (Fig. 2E, F). RT4-p53DD cells predominantly invaded as cohesive cell clusters, consistent with their characteristic clustered growth pattern. In contrast, T24 cells showed both clustered invasion and scattered individual invading cells within the 14-day observation period, which were markedly reduced by ectopic FAM193A expression (Fig. 2G, H). Together, these findings further support a suppressive role of FAM193A in BC cell invasion in a tissue context. Notably, although known for their invasive capacity in Boyden chamber assay, BFTC-905 cells showed no detectable invasion within the 14-day observation period, irrespective of FAM193A expression (Fig. S2C), suggesting that this cell line may be less suitable for this *ex vivo* invasion model.

Since alterations in cell-cell adhesion often lead to invasive behaviour, we next used the hanging drop assay to examine the effect of FAM193A on cell aggregation. Lack of FAM193A reduced the formation of tight cell aggregates of RT4-p53DD cells, whereas ectopic expression of FAM193A promoted tighter cell aggregation of T24 and BFTC-905 cells (Fig. 2I).

Collectively, these findings establish FAM193A as a negative regulator of BC cell migration and invasion and suggest that enhanced cell-cell cohesion may contribute to its anti-invasive activity. We next investigated the molecular mechanisms underlying these effects.

FAM193A is constitutively degraded under normal growth conditions but accumulates upon DNA damage

During our experiments, we first observed that following transfection of HEK293T cells with V5-tagged FAM193A protein (V5-FAM193A, abbreviated as V5 in the figures), FAM193A protein levels were initially very high, for example at days 2 or 3 post-transfection, but rapidly declined to very low levels during selection (Fig. 3A, top; Fig. S3A). Notably, although *FAM193A* mRNA levels were comparable at 48 hours and 2 weeks post-transfection, protein levels were dramatically reduced during blasticidin selection (Fig. 3A, bottom). In addition, in

559 cells expressing high levels of FAM193A, the V5 antibody detected multiple lower-molecular-
560 weight bands, suggesting the presence of FAM193A degradation products (Fig. S3A). Second,
561 the observed molecular weight of FAM193A was substantially higher (~230 kDa) than its
562 predicted molecular weight (~140 kDa). These results indicated a post-transcriptional
563 regulation of FAM193A protein levels. This assumption is supported by the observations, that
564 even though *FAM193A* mRNA is widely expressed in a variety of cell lines under normal growth
565 conditions, both endogenous and stably expressed ectopic FAM193A proteins are hardly
566 detectable, prompting us to investigate whether FAM193A abundance is regulated at the level
567 of protein stability. To this end, FAM193A-V5 stably expressing HEK293T cells were treated
568 with the proteasome inhibitor MG132, in order to examine if the protein degradation observed
569 in FAM193A overexpression cells is regulated by proteasome machinery. Notably, K48-linkage
570 specific anti-ubiquitin antibodies, indicative of ubiquitin mediated protein degradation, are
571 detectable in FAM193A expressing cells specifically (Fig. S3B, top), while non-ubiquinated
572 FAM193A proteins are detectable in anti-V5 pulldowns (Fig. S3B, bottom), suggesting that the
573 V5-antibody pulls down mainly FAM193A, which is not targeted for degradation. Moreover,
574 based on the previous reports showing an association of FAM193A with p53, we treated cells
575 with the DNA-damage inducing agent doxorubicin [9]. As indicated above (Fig. 3A), initially
576 high levels of ectopic FAM193A are degraded to normal growth levels during culturing in
577 HEK293T cells. Our results show that FAM193A protein levels rapidly accumulate following
578 MG132 treatment, indicating that FAM193A undergoes constitutive proteasome-dependent
579 degradation (Fig. 3B). To exclude the possibility that MG132 indirectly affects transgene
580 transcription, cells were treated with actinomycin D to block RNA synthesis. Notably, MG132
581 still induced substantial accumulation of FAM193A protein in the presence of actinomycin D,
582 despite of lower *FAM193A* mRNA levels (MG132 + ActD), suggesting that this effect primarily
583 results from inhibition of protein degradation rather than increased transcription (Fig. 3B).
584 Importantly, doxorubicin-induced DNA damage similarly caused a marked increase in
585 FAM193A protein abundance (Fig. 3B).

We next investigated if FAM193A protein stability is similarly regulated in BC cells. In both T24 and BFTC-905 cells, following selection of cells for stable expression, ectopic FAM193A protein was barely visible, despite readily detectable *FAM193A* mRNA expression (Fig. 3C, D). Notably, consistent with the findings in HEK293T cells, both MG132 and doxorubicin markedly increased FAM193A protein levels, while MG132-induced accumulation remained largely unaffected by actinomycin D treatment, further supporting a post-transcriptional regulation of FAM193A levels (Fig. 3C, D; Fig. S3C). We also examined potential influence of growth signalling and oxidative stress in parallel to DNA damage and MG132-treatment on FAM193A protein stability using epidermal growth factor (EGF) and hydrogen peroxide (H_2O_2)-treatment, respectively. In contrast to MG132- or doxorubicin treatments, neither EGF- nor H_2O_2-treatment significantly affected FAM193A expression (Figs. S3C and S3D).

Together, these findings indicate that FAM193A is continuously degraded under normal growth conditions but becomes stabilized in response to DNA damage.

To delineate the subcellular localization of FAM193A, we first performed Western blot experiments with protein extracts from cytosolic and nuclear fractions. Under standard fractionation conditions, FAM193A was readily detected in nuclear extracts. However, increasing the NP40 concentration and optimizing the centrifugation conditions progressively reduced the amount of FAM193A detected in the nuclear fraction while increasing its recovery in the cytoplasmic fraction (Fig. 3E). Using Calnexin (marker for endoplasmic reticulum) and, VDAC1/3 (mitochondrial marker), we observed that the nuclear fraction still contained high levels of impurity or nucleus associated organelles, whereas the cytoplasmic fraction was essentially free of nuclei, as shown by Lamin A/C antibody (Fig. 3E). These findings suggested that the apparent nuclear localization of FAM193A may result from contamination of the nuclear fraction by organelle-associated structures.

Given the limitations of subcellular fractionation and the observation that FAM193A protein levels increase following DNA damage, we further examined its localization by immunofluorescence microscopy. FAM193A displayed a predominantly cytoplasmic

distribution with no detectable nuclear signal and showed no obvious colocalization with markers of the Golgi apparatus (visualized by anti-GM130), autophagosomes (visualized by anti-LC3 A/B), mitochondria (visualized by anti-TOM20), nuclear envelope (visualized by anti-Lamin A/C) or F-actin, but a partial colocalization with the perinuclear endoplasmic reticulum, as indicated by Calnexin staining (Fig. 3F). Together, these findings indicate that FAM193A is predominantly distributed throughout the cytoplasm, while partially colocalizing with the perinuclear endoplasmic reticulum under normal growth conditions. Interestingly, DNA damage induced a remarkable redistribution of FAM193A. Strikingly, treatment with doxorubicin for 24h resulted in the formation of prominent cytoplasmic aggregates (Fig. 3G). Quantitative analysis revealed that 52.5% FAM193A-positive cells formed aggresome-like structures (Fig. 3G). Notably, Calnexin is known to form aggresomal structures with p62 (also known as sequestosome 1: SQSTM1, alternative description: p62/SQSTM1), a central adapter protein, which plays a key role in the formation and degradation of aggresomes in response to DNA-damage response and autophagy [42, 43]. Thus, we next examined whether the FAM193A-positive aggresome-like structures were associated with p62. Under normal growth conditions, only limited colocalization was observed between the two proteins, while FAM193A and p62 exhibited markedly increased colocalization upon doxorubicin treatment in both HEK293T and HeLa cells, with near-complete overlap in a subset of aggregates (Fig. 3H). FAM193A-V5 specifically interacted with endogenous p62 under normal growth conditions, and this interaction was further enhanced following 24 h of doxorubicin treatment (Fig. 3I). Notably, the interaction between p62 and FAM193A was detected by the results of the reciprocal IPs using either anti-V5 or anti-p62 antibodies. Of note, the previously reported interaction between FAM193A and MDM4 was readily detected and served as a positive control for IPs [9]. We next investigated the potential relationship between FAM193A and p62. Ectopic expression of FAM193A increased p62 phosphorylation at Ser349, whereas loss of p62 resulted in increased FAM193A levels under both normal growth conditions and, more prominently, following doxorubicin treatment, suggesting that FAM193A degradation is

impaired in the absence of p62. Consistent with impaired FAM193A degradation, higher-molecular-weight FAM193A species accumulated in p62-deficient cells (Fig. 3J).

FAM193A, P65 and PHD3 form a regulatory complex

To investigate the molecular mechanisms by which FAM193A suppresses BC cell migration and invasion, we first examined several canonical signalling pathways implicated in BC progression. Immunoblot analysis revealed that FAM193A overexpression had limited effects on AKT, ERK and STAT3 pathway activation, whereas the expression of FAK, YAP and multiple cytoskeleton-associated proteins remained largely unchanged in T24 and BFTC-905 cells irrespective of FAM193A expression (Fig. S4A–C). In contrast, phosphorylation of P65 at Ser536 and p62 at Ser349 was markedly altered in HEK293T, T24 and BFTC-905 cells, suggesting that NF-κB signalling and p62-associated response pathways may contribute to the biological functions mediated by FAM193A (Fig. 3J, Fig. 4A and Fig. S4D). Interestingly, although FAM193A markedly reduced phosphorylation of P65 at Ser536, phosphorylation of IKKα/β and IκBα remained largely unchanged, indicating that FAM193A does not primarily regulate NF-κB through the canonical IKK–IκBα cascade but instead acts at the level of P65 or associated regulatory complexes (Fig. 4A).

To identify proteins that might connect FAM193A with NF-κB signalling and p62-associated cellular responses, we integrated the reported interaction networks of FAM193A, p62 (*SQSTM1*), P65 (*RELA*) and IκBα (*NFKBIA*) using the BioGRID database. Intersection analysis identified PHD3 (*EGLN3*) as the only common candidate shared by all four interaction networks (Fig. 4B). Firstly, using proximity ligation assays (PLA), we revealed abundant PLA signals, indicative of FAM193A/PHD3 colocalization, predominantly in the cytoplasm, supporting a physical interaction between FAM193A and PHD3 (Fig. 4C). To further investigate the interaction between FAM193A and PHD3, we ectopically expressed both proteins in HEK293T cells and performed V5 immunoprecipitation. Exogenous PHD3 efficiently co-immunoprecipitated with FAM193A, confirming their physical association (Fig. S4E). Having established a physical interaction between FAM193A and PHD3, we next

investigated whether FAM193A influences PHD3 protein stability and vice versa. In HEK293T cells, depletion of FAM193A reduced basal PHD3 protein levels and attenuated DNA damage-induced PHD3 accumulation (Fig. 4D). Similar results were obtained in RT4-p53DD cells upon CRISPR-Cas9 mediated knockout of FAM193A using pool of FAM193A knockout cells (Fig. 4E) and independently derived single clones of FAM193A knockout cells, while the impact of FAM193A on PHD3 stability in response to hypoxic stress was rather mild (Fig. 4F).

We next performed co-immunoprecipitation assays in HEK293T cells expressing V5-tagged FAM193A in order to examine the association of P65 with FAM193A and PHD3. Notably, P65-PHD3 interaction was previously reported [23]. We find that endogenous P65 specifically co-immunoprecipitated with FAM193A, identifying P65 as a previously unrecognized FAM193A-associated protein (Fig. 4G), in addition to the above described p62-FAM193A interactions (Fig. 3I). Because endogenous PHD3 (~27 kDa) could not be reliably detected in V5-FAM193A immunoprecipitates owing to interference with immunoglobulin light chains, we performed reciprocal immunoprecipitation using an anti-PHD3 antibody. FAM193A was readily detected in PHD3 immunoprecipitates under normal growth conditions, and this interaction was significantly enhanced following doxorubicin treatment ($P = 0.008$; Fig. 4G). Our results further indicated that FAM193A overexpression increased the association between PHD3 and P65 under both normal growth and DNA damage conditions, suggesting that FAM193A promotes the assembly or stability of the PHD3–P65 complex (Fig. 4G). Given that FAM193A overexpression enhanced the association between PHD3 and P65 (Fig. 4C), we next investigated whether all three proteins coexist within a common complex. Using HEK293T cells stably expressing EV or PHD3 and transiently transfected with EV or FAM193A-V5, we first immunoprecipitated PHD3 and subsequently re-immunoprecipitated P65 from the non-denaturing eluate of the initial PHD3 pulldown. FAM193A-V5 was detected in the subsequent immunoprecipitation from PHD3-overexpressing cells transiently expressing FAM193A-V5. Notably, FAM193A overexpression enhanced the association between PHD3 and P65, supporting the presence of all three proteins within a common complex (Fig. 4H).

Collectively, these findings identify P65 and PHD3 as FAM193A-associated proteins, in addition to p62, and establish FAM193A as a positive regulator of PHD3 stability and PHD3–P65 complex formation during cellular stress responses.

FAM193A regulates dynamic PHD3–P65 complex assembly and restrains NF-κB activation

Given that the stress stimuli examined above are not canonical activators of the NF-κB signalling pathway, we next used TNFα stimulation to investigate the potential relationship among FAM193A, PHD3, and P65 during canonical NF-κB activation. HEK293T cells expressing V5-tagged FAM193A were treated with TNFα, and immunoprecipitation analyses were performed (Fig. 5A). The results demonstrated that FAM193A stably associates with the non-phosphorylated P65, while Ser536-phosphorylated P65 (Ser536-p-P65), which is linked to NF-κB transcriptional activity, was not detectable in association with FAM193A, suggesting that FAM193A preferentially interacts with the transcriptionally inactive P65. Whether FAM193A directly promotes or facilitates dephosphorylation of Ser536-p-P65 remains to be determined. Reciprocal immunoprecipitation experiments using either anti-PHD3 or anti-P65 antibodies for IP further confirmed the interactions among FAM193A, PHD3, and P65 (Fig. 5A). Importantly, TNFα stimulation markedly altered these interactions: quantitative analysis of the IP-Western results revealed that FAM193A-P65 and FAM193A-PHD3 associations peaked at 30 min of TNFα stimulation (Fig. 5A, Fig. S5A) while P65-IKBα interaction was completely lost at this time-point (Fig. 5A), another indicative of P65 phosphorylation and NF-κB pathway activation. Notably, FAM193A levels were inversely correlated with P65-IKBα association, suggesting that FAM193A impairs this interaction during the early phase of TNFα stimulation (note the 0, 10, and 30 min time-points in P65 IPs in Fig. 5A and Fig. S5A). Independent experiments with extended TNFα-treatment time-periods confirmed the dynamics interactions of both FAM193A–P65 and FAM193A–PHD3 interactions in response to TNFα-treatment (Fig. S5B). Interestingly, long-term treatment with TNFα stabilized FAM193A levels, although the

consequence of this observation was not further investigated in this study and needs to be elucidated in future studies.

To further examine the relationship between FAM193A, PHD3 and P65, we overexpressed PHD3 in the absence and presence of ectopic FAM193A in HEK293T cells, which have low endogenous levels of both proteins. Firstly, the results of IP-WB experiments clearly confirmed the dynamic interaction between FAM193A and PHD3 during TNFα stimulation (Fig. 5B). Importantly, in the absence of ectopic FAM193A, PHD3 associated with both non-phosphorylated P65 and Ser536-p-P65, while PHD3- Ser536-p-P65 interaction was no longer detectable in cells with ectopic FAM193A expression. On the other hand, PHD3 interaction with the non-phosphorylated P65 was readily detectable in IPs of cells with ectopic FAM193A. Moreover, these interactions were inversely regulated in response to TNFα treatment. In mock-treated control cells, PHD3 showed stronger association with non-phosphorylated P65 and minimal interaction with Ser536-phosphorylated P65. By contrast, at 10 and 20 min after TNFα stimulation, the interaction between PHD3 and Ser536-phosphorylated P65 increased, whereas the association between PHD3 and non-phosphorylated P65 decreased (Fig. 5B). These findings suggest that FAM193A impairs the interaction between PHD3 and Ser536-p-P65 and suppresses canonical NF-κB pathway activity. Conversely, PHD3 depletion (Fig. S5C) impairs FAM193A-P65 interactions (Fig. S5D), supporting the idea of coordinated function of FAM193A-PHD3 on NF-κB signalling.

To examine the temporal and spatial dynamics of the FAM193A-PHD3–P65 interactions in cells in response to TNFα stimulation, we performed proximity ligation assays (PLA) in the presence or absence of PHD3. It is important to note that an anti-P65 antibody was used for these experiments that detects total P65 (including both non-phospho P65 and anti-Ser536-p-P65), as the anti-Ser536-p-P65 antibody was not suitable for the PLA assays. As we observe the increase of nuclear P65 signals in response to TNFα stimulation, we consider the nuclear PLA signals as colocalized PHD/Ser536-p-P65 signals, although we do not exclude the presence of non-phospho P65 in the nucleus. Under normal growth conditions, PHD3–P65

PLA signals were mainly localized in the cytoplasm. At 10 min after TNFα stimulation, distinct nuclear PLA signals were observed, suggesting that a fraction of the PHD3–P65 complex (i.e. PHD/Ser536-p-P65) enters the nucleus upon NF-κB activation, in line with a previous report showing that PHD3 binds to P65 and co-localizes with nuclear P65 following TNFα stimulation [23]. As stimulation continued, nuclear PLA signals gradually decreased and cytoplasmic signals again became predominant (Fig. 5E). PHD3 knockdown markedly reduced the overall PLA signal and abolished the transient nuclear PLA signal observed after TNFα stimulation (Fig. S5E), confirming the specificity of the interaction. In contrast, PLA signals for both FAM193A–P65 (Fig. 5C) and FAM193A–PHD3 (Fig. 5D) remained predominantly cytoplasmic, with no obvious nuclear localization. To further determine whether PHD3 regulates NF-κB nuclear accumulation, we performed nuclear-cytoplasmic fractionation followed by PHD3 immunoprecipitation. PHD3–P65 binding was detected in both cytoplasmic and nuclear fractions. Interestingly, PHD3 overexpression reduced TNFα-induced nuclear accumulation of P65 and P50, as confirmed by quantification of nuclear P65 and P50 levels (Fig. 5F and Fig. S5F), indicating that PHD3 negatively regulates NF-κB nuclear accumulation.

Collectively, these findings support a model in which FAM193A preferentially associates with non-phosphorylated P65, limits the interaction between PHD3 and transcriptionally active P65 (i.e. Ser536-p-P65), acting as a modulator of NF-κB signalling.

FAM193A suppresses sustained P65 activation downstream of IKK–IκB signalling

Given the dynamic and cyclic activation of TNFα-induced P65 and the observed stabilization of FAM193A at 24h TNFα treatment, we extended the duration of TNFα stimulation to examine the effect of FAM193A on the sustained activation phase of NF-κB signalling. In HEK293T cells, FAM193A overexpression markedly impaired phosphorylation of P65 at Ser536 following prolonged TNFα stimulation; quantitative analysis of the time-course changes revealed a statistically significant overall difference (two-way ANOVA, $P < 0.0001$; Fig. 6A). In contrast, protein levels and/or phosphorylation of classical NF-κB -upstream signalling molecules, such

as p-IKKα/β and p-IκBα, remained largely unaffected. Notably, FAM193A overexpression was accompanied by elevated PHD3 protein levels.

Importantly, FAM193A overexpression in HEK293T cells (lanes 1-3 in Fig. 6B: FAM193A-V5-gGFP) resulted in a marked reduction of TNFα-induced Ser536p-P65 levels compared to empty vector containing control cells (lanes 4-6 in Fig. 6B: EV-gGFP). Conversely, CRISPR-Cas9-mediated FAM193A knockout using two independent FAM193A-targeting gRNAs (lanes 7-9 and 10-12, respectively: gFAM193A#1 and gFAM193A#2) restored TNFα-induced Ser536 phosphorylation of P65 (see lanes 7-12 versus lanes 1-3 in Fig. 6B), confirming that FAM193A impairs accumulation of transcriptionally active pSer536-P65. This conclusion is supported by the results of knockout studies of endogenous FAM193A in the BC cell line RT4-p53DD (Fig. 6C). TNFα treatment resulted in elevated pSer536-P65 levels in FAM193A knockout RT4-p53DD cells, compared to RT4-p53DD cells with a GFP targeting control guide RNA (gGFP). Notably, pSer536-P65 levels remained persistently elevated following prolonged stimulation in FAM193A knockout cells, with overall time-course analysis showing a significant difference compared to the gGFP containing cells (two-way ANOVA, $P < 0.0001$; Fig. 6C); meanwhile, levels of p-IKKα/β and p-IκBα did not show a consistent increase. The inhibitory effect of FAM193A on TNFα-induced P65 activation in the BC cell lines was also investigated using T24 and BFTC-905 cells. Consistent with the HEK293T model, FAM193A overexpression reduced P65-Ser536 phosphorylation levels following TNFα stimulation. This effect reached statistical significance in BFTC-905 cells (two-way ANOVA, $P = 0.0001$). A similar trend was observed in T24 cells, although the differences were not statistically significant (two-way ANOVA, $P = 0.047$) (Fig. 6D, E). Meanwhile, no consistent changes were observed in the phosphorylation levels of IKKα/β and IκBα. Collectively, these results indicate that the inhibitory effect of FAM193A on sustained P65 activation is not cell line specific, further supporting the conclusion that FAM193A restricts NF-κB activation primarily by promoting the termination of P65 signalling.

To determine whether the inhibitory effect of FAM193A on NF-κB signalling is mediated by PHD3, endogenous PHD3 was depleted in HEK293T cells, which ectopically express FAM193A (HEK293T-FAM193A). In line with above presented results, FAM193A markedly reduced TNFα-induced phosphorylation of P65 at Ser536 (HEK293T-FAM193A cells with a scrambled control shRNA). In contrast, PHD3 knockdown (HEK293T-FAM193A cells with a shPHD3 shRNA) substantially attenuated the suppressive effect of FAM193A on P65 phosphorylation (see 30 minute and 120 minute TNFα-treatment time-points in the presence of FAM193A), resulting in increased accumulation of Ser536-phosphorylated P65 following TNFα stimulation (Fig. 6F). These findings suggest that PHD3 mediates, at least in part, suppression of sustained NF-κB activation by FAM193A.

To further elucidate the mechanism by which FAM193A regulates NF-κB signalling, we first examined the effect of FAM193A on NF-κB transcriptional activity under various stimulation conditions. A luciferase reporter assay using the 3×κB-promoter demonstrated that doxorubicin or TNFα treatments significantly induced NF-κB activity in EV-containing cells, while FAM193A overexpression markedly inhibited doxorubicin or TNFα-induced reporter activation (Fig. 6G). On the other hand, hypoxia or H_2O_2 treatment did not significantly induce reporter activity and the impact of FAM193A under these conditions was limited (Fig. 6G). We next examined the combined effects of FAM193A and PHD3 on NF-κB transcriptional activity using the reporter assay. Please note that due to robust overexpression of FAM193A alone produces near-maximal inhibition of reporter activity under the experimental conditions, the amount of FAM193A expression plasmid was reduced by 50% to avoid saturation and enable assessment of the contribution of co-expressed PHD3. This design allowed us to evaluate the relative contribution of PHD3 when co-expressed with FAM193A. Under these conditions, expression of either FAM193A or PHD3 alone reduced TNFα-induced NF-κB reporter activity (Fig. 6H). Co-expression of FAM193A and PHD3 did not produce a further reduction in reporter activity compared with either factor alone under these conditions, consistent with the possibility that FAM193A and PHD3 act through a common or convergent regulatory mechanism (Fig. 6H). These findings indicate that FAM193A suppresses NF-κB transcriptional activity under

conditions that robustly activate the reporter, whereas little effect was observed under hypoxia or H_2O_2 treatment, consistent with the weaker NF-κB activation induced by these stimuli in this experimental system.

Finally, we examined the impact of different FAM193A deletion constructs on NF-κB reporter activity in order to identify the functional domains of FAM193A relevant for the regulation of NF-κB signalling (Fig. 6I). The results of the reporter assays showed that full-length FAM193A and constructs 3, 4, and 4.5 (indicated by Fr3, Fr4 and Fr4.5, respectively) reduced TNFα-induced NF-κB activity, with Fr4 exhibiting the most pronounced inhibitory effect (Fig. 6I). IP-WB experiments using Halo-tagged FAM193A expression constructs revealed that full-length FAM193A, Fr3, and Fr4 bound strongly to P65 (Fig. 6J), correlating with their respective capacities to inhibit the NF-κB reporter activity (Fig. 6I). Given the association of PHD3 with FAM193A and P65, we also investigated which FAM193A domains mediate the interaction with PHD3 and their relation to NF-κB reporter activity. For this purpose, we conducted IP experiments in cells with ectopic PHD3 in combination with ectopically expressed Halo-tagged FAM193A constructs; these assays confirmed that full-length FAM193A, Fr4 and to lesser extent Fr3 bound robustly to PHD3 (Fig. 6K). Collectively, these results indicate that the inhibition of NF-κB signalling by FAM193A is linked to the structural domains that mediate its interaction with P65 and PHD3.

FAM193A restrains BC cell invasion and migration downstream of NF-κB activation

As we have identified FAM193A in a screen to identify genes and molecular pathways, which regulate cancer cell migration and invasion, it is crucial to evaluate the relationship between FAM193A and NF-κB in this context. Previous reports already indicated that TNFα-treatment may increase cancer-cell migration, invasion, and related metastatic phenotypes of cancer cells of different origin of cancer [44-47]. To evaluate the effect of TNFα-induced NF-κB activation on the invasive capacity of BC cells, first non-/low-invasive BC cell line RT4 cells were treated with increasing concentrations of TNFα and the invasive capacity of these cells was evaluated by Boyden chamber assays. The results of these experiments revealed that

TNFα promoted the migratory/invasive capacity of RT4 cells, with a concentration-dependent increase reaching the strongest effect at 10 ng mL^{-1} (Fig. 7A, B). Notably, the impact of TNFα on RT4 cell migration/invasion capacity declined at higher concentrations, likely due to impairment of cell viability (Fig. 7C).

In order to assess whether this process depends on NF-κB signalling, we used two independent shRNAs to knockdown P65 in RT4 cells (Fig. 7D) and performed Boyden chamber assays (Fig. 7E). Since the Boyden chamber assay lasted 6 days, fresh medium containing TNFα was replenished every 48 hours during the experiment. To verify the stability of P65 knockdown under long-term treatment conditions, we collected cells under the same treatment regimen for Western blot analysis. The results showed that both shRNAs stably reduced P65 protein levels throughout the experiment (Fig. 7F). Boyden chamber assays demonstrated that in line with the above results (Fig. 7A), TNFα-treatment significantly promoted invasive capacity of RT4 parental cells, whereas P65 knockdown markedly attenuated this effect (Fig. 7E), indicating that TNFα-induced invasion primarily depends on the NF-κB signalling pathway.

Given that the aforementioned results indicate that FAM193A can restrict NF-κB activation, we further examined its effect on the TNFα-induced invasion phenotype. For this purpose, RT4-p53DD cells with CRISPR-Cas9-mediated FAM193A knockout were used. TNFα significantly promoted cell invasion in RT4-p53DD cells with control gRNAs (RT4-p53DD-gGFP#1 or RT4-p53DD-gGFP#2, respectively), while FAM193A deficiency (RT4-p53DD-gFAM193A-16363#1 or RT4-p53DD-gFAM193A-16363#2, respectively) further enhanced TNFα-induced invasion (two-way ANOVA interaction $P = 0.0032$), and both independent knockout clones exhibited consistent results (Fig. 7G, H). Similarly, in scratch assays, FAM193A deficiency promoted cell migration and further enhanced the TNFα-induced migratory response (Fig. 7I, J). These results demonstrate that loss of FAM193A enhances both basal and TNFα-induced invasion and migration, supporting a role for FAM193A as a negative regulator of these phenotypes.

To further investigate the relationship between FAM193A and NF-κB-related transcriptional programs, we first analysed potential correlations between *FAM193A* and NF-κB target gene expressions in the GSE32894 cohort [48]. *FAM193A* expression was negatively correlated with several NF-κB-responsive genes, including *PTGS2*, *RELB*, *TNF*, *IL8* and *CXCL10* (Fig. 7K), suggesting an inverse association between FAM193A and NF-κB-related transcriptional output.

To validate this relationship in an independent cohort, we next analysed single-cell RNA-sequencing data using another human dataset (GSE269877 cohort), comprising 27 samples from 23 patients [33]. Urothelial cells were aggregated into sample-level pseudo-bulk profiles, and one profile was retained per patient, resulting in 23 independent patient-level profiles for analysis**.** *FAM193A* expression was negatively correlated with all six selected NF-κB-related genes, with the strongest associations observed for *CXCL8 (IL8)* (rho = −0.57, FDR = 0.029), *CXCL1* (rho = −0.49, FDR = 0.038) and *CXCL3* (rho = −0.49, FDR = 0.038) (Fig. 7L). These associations remained negative after adjustment for BCG-naïve versus recurrent sample status (Fig. 7M). A selected six-gene *RELA*-positive target score showed a strong inverse correlation with *FAM193A* (rho = −0.66, $P < 0.001$; Fig. 7N), whereas the broader *RELA*-positive target score showed only a weaker association (rho = −0.36, P = 0.091; Fig. 7O). Permutation analysis further showed that the six-gene association was stronger than expected from random *RELA*-positive target sets (P = 0.0039; Fig. 7P).

Having observed a consistent inverse relationship in two independent human datasets, we next tested whether FAM193A directly affects the expression of these NF-κB-responsive genes in BC cells. In RT4-p53DD cells, FAM193A deletion selectively enhanced the expression of *IL8*, *PTGS2*, *CXCL1* and *CXCL3*, whereas *IL1B* and *CXCL10* were not significantly affected (Fig. 7Q). Conversely, in T24 and BFTC-905 cells, FAM193A overexpression reduced the expression of a subset of NF-κB-responsive genes, with *IL8* showing the most consistent decrease, while changes in the remaining genes were relatively

limited (Fig. S6J, K). Collectively, these findings support an inverse relationship between FAM193A and selected NF-κB transcriptional outputs in human BC and experimental models.

The impact of FAM193A and NF-κB was also investigated in aggressive BC cell lines, which express low/no FAM193A. Overexpression of FAM193A impaired the invasion and migration capacity of T24 cells compared to control cells with an empty vector, but this inhibitory effect was independent of TNFα, likely due to high levels of the ectopic FAM193A protein (Fig. S6A-D). Similarly, overexpression of FAM193A significantly reduced the invasion capacity of BFTC-905 cells (Fig. S6E, F), but had only a minor impact on the migration capacity of these cells in the scratch assay (Fig. S6G, H). TNFα slightly promoted invasion and migration both in control BFTC-905 cells with an empty vector as well as in BFTC-905 cells with ectopic FAM193A (Fig. S6E-H). In both cell lines, TNFα-treatment had a minor effect on cell viability (Fig. S6I). Consistent with these phenotypic differences, TNFα failed to induce the NF-κB downstream targets CXCL1 and CXCL3 in T24 cells, whereas only a modest induction was observed in BFTC-905 cells (Fig. S6J, K). In addition, both T24 and BFTC-905 cells exhibited higher basal expression levels of CXCL1 and CXCL3 than RT4 cells prior to TNFα stimulation. Given that CXCL1 and CXCL3 have previously been implicated in promoting cancer-cell invasion, migration, and metastatic progression, the limited TNFα-induced upregulation of these chemokines, despite their relatively high basal expression, may partly explain the weak responsiveness of T24 and BFTC-905 cells to TNFα compared with RT4 cells [49-51]. Overall, although different BC cell lines exhibited varying degrees of responsiveness to TNFα stimulation, FAM193A consistently demonstrated an inhibitory effect on cell motility.

Consistent with an inhibitory role of PHD3 in BC cell invasion, knockdown of PHD3 significantly enhanced the invasive capacity of RT4 cells (Fig. S6L). However, ectopic expression of PHD3 only mildly reduced the invasive capacity of T24 cells (Fig. S6M). A likely explanation for this mild effect may be due to the high expression of CXCL1 and CXCL3, as discussed above.

In order to examine whether FAM193A and PHD3 cooperate during TNFα-induced regulation of cancer cell invasion, we ectopically overexpressed both factors in BFTC-905 cells for stable

933 expression. BFTC-905 cell pools stably expressing FAM193A alone, PHD3 alone, or both
934 proteins were generated (Fig. S6N, left). Although ectopic expression of either FAM193A or
935 PHD3 alone reduced cell invasion, neither of them completely prevented the TNFα-induced
936 increase in invasive capacity. In contrast, co-expression of FAM193A and PHD3 markedly
937 suppressed invasion under both basal and TNFα-stimulated conditions, with no apparent
938 increase following TNFα treatment (Fig. S6N, middle and right). To further validate these
939 findings, single-cell clones were isolated from the FAM193A/PHD3 double-overexpression
940 pool (Fig. S6O, left). Two double-positive clones and two independent EV control clones were
941 subsequently selected for functional analysis. Both double-positive clones strongly reduced
942 invasive capacity of BFTC cells, both under untreated and TNFα-stimulated conditions,
943 consistent with the results obtained using pooled cells (Fig. S6O).

Discussion

This study identifies FAM193A as a previously unrecognised suppressor of BC cell invasion and provides a mechanistic framework linking FAM193A proteostasis to the control of NF-κB signalling. FAM193A was discovered through a functional RNAi screen designed to select RT4 cells that acquired invasive capacity after gene depletion. Subsequent analyses converged on a consistent phenotype: FAM193A expression was lower in highly invasive BC cell lines compared to low/non-invasive BC cell lines, as well as in MIBC than in NMIBC. Notably, reduced *FAM193A* expression in patients with MIBC was associated with poorer survival. Functional experiments revealed that FAM193A loss enhanced migration and invasion and weakened cell aggregation, whereas ectopic FAM193A suppressed motility and promoted compact aggregates without measurably altering cell viability. The functional data, combined with the reduced FAM193A levels observed in human tumours and BBN-induced mouse bladder cancers, suggest that FAM193A loss may be associated with, and potentially promote, progression to an invasive phenotype.

A notable finding is that FAM193A abundance is controlled predominantly at the post-transcriptional level. Stable expression produced readily detectable FAM193A transcripts but only low protein abundance, whereas proteasome inhibition rapidly restored the protein even when transcription was blocked. The accumulation of K48-linked ubiquitin species and lower-molecular-weight FAM193A products further supports constitutive ubiquitin–proteasome-dependent turnover. Rapid degradation may provide a means to keep the activity of this large protein low under normal growth conditions while permitting its acute accumulation in response to stress conditions. Doxorubicin induced FAM193A stabilisation in several cell backgrounds, whereas EGF and hydrogen peroxide had limited effects under the conditions tested. Thus, FAM193A does not appear to be a generic sensor of growth-factor or oxidative signalling; instead, its stabilisation may be preferentially coupled to DNA damage or to a subset of proteotoxic responses. Increased FAM193A stabilisation during long-term TNFα treatment also suggests a potential role of this protein in inflammatory conditions.

This stress responsiveness is in accordance with the reported connection between FAM193A and the p53 pathway [9]. However, the present data do not establish that p53 is required for FAM193A stabilisation or for its anti-invasive activity, particularly because key experiments were performed both in p53-proficient cells (e.g. BFTC-905) as well as in p53 deficient cells (T24, RT4-p53DD) cells with similar outcomes. Rather, they suggest that FAM193A may function at the intersection of multiple stress-response systems. DNA damage caused a striking reorganisation of FAM193A from a diffuse cytoplasmic distribution into reticular and aggregate-like structures that overlapped with p62/SQSTM1. p62 is a multifunctional scaffold that links ubiquitinated cargo to selective autophagy and is a prominent component of aggresomes and stress-induced protein condensates [42, 52, 53]. The physical association between FAM193A and p62, together with enhanced colocalisation after doxorubicin treatment, supports recruitment of stabilised FAM193A into a p62-organised protein-quality-control compartment. The increased abundance of FAM193A species in p62-deficient cells is consistent with a contribution of p62 to FAM193A turnover, although the directionality and functional consequences of this relationship require further resolution. The aggregate phenotype should therefore be interpreted cautiously. FAM193A-positive structures may represent aggresomes, autophagic cargo-processing sites or stress-induced assemblies that concentrate signalling proteins. Current data do not establish whether aggregate formation is necessary for FAM193A-mediated suppression of NF-κB or invasion.

Mechanistically, our results place PHD3 and P65 at the centre of FAM193A function. FAM193A interacted with both proteins, enhanced the abundance of PHD3 and promoted formation of a PHD3–P65 complex during stress. Importantly, results of sequential immunoprecipitation experiments provided compelling evidence for the simultaneous presence of FAM193A, PHD3, and P65 within a common protein complex, supporting their coordinated association beyond individual pairwise interactions. On the other hand, loss of FAM193A reduced basal PHD3 levels and attenuated its accumulation after doxorubicin treatment in independent genetic models. PHD3 was originally defined as an oxygen-sensing HIF prolyl hydroxylase [22], but

subsequent work has demonstrated broader functions in inflammatory and tumour signalling [23-27]. Reports describing PHD-dependent inhibition of IKKβ or interaction with the IKK complex provide one route by which PHD proteins can restrain NF-κB [24, 25]. In the present study, however, FAM193A altered sustained P65 Ser536 phosphorylation without consistently changing IKKα/β or IκBα phosphorylation. This distinction suggests that the FAM193A–PHD3 module acts primarily at the level of P65 or a P65-associated complex rather than by globally suppressing canonical pathway initiation. The temporal interaction data further support a role in signal resolution. FAM193A preferentially associated with non-phosphorylated P65, whereas interaction with Ser536-phosphorylated P65 was not detected. TNFα stimulation dynamically altered FAM193A–PHD3–P65 complex assembly, and FAM193A expression limited the association between PHD3 and phospho-P65. In parallel, FAM193A reduced prolonged P65 Ser536 phosphorylation and NF-κB reporter activity, while FAM193A deletion prolonged P65 activation. One model is that FAM193A stabilises PHD3 and organises a cytoplasmic complex that retains, remodels or promotes dephosphorylation of activated P65 after the initial response. The observation that PHD3 overexpression reduced nuclear P65 and P50 is consistent with enhanced nuclear export or cytoplasmic sequestration, although direct measurements of nucleocytoplasmic transport are needed. An alternative, not mutually exclusive, model is that FAM193A shifts PHD3 substrate selection or scaffolding behaviour away from transcriptionally active P65, thereby favouring pathway termination.

Whether the hydroxylase activity of PHD3 is required remains unresolved. PHD3 can influence NF-κB through catalytic and non-catalytic mechanisms, and reported effects vary by cell type [23-25]. The present experiments demonstrate interaction and stabilisation but do not identify a hydroxylated residue on FAM193A, P65 or another complex member. Catalytically inactive PHD3 mutants, hydroxylation-sensitive mass spectrometry and rescue experiments in PHD3-depleted cells will be necessary to distinguish enzymatic from scaffolding functions. Similarly, FAM193A truncation analyses identify regions that correlate with PHD3/P65 binding and

reporter inhibition, but higher-resolution mapping is required to define minimal interaction motifs and to separate effects of expression level, folding and stability.

The signalling findings are functionally connected to invasion. TNFα promoted RT4 cell invasion in a P65-dependent manner, FAM193A deficiency amplified TNFα-induced migration and invasion, and FAM193A altered a subset of NF-κB-responsive genes, including IL8, PTGS2, CXCL1 and CXCL3. These genes encode inflammatory mediators that can reinforce tumour-cell motility and shape the local microenvironment. Prior studies have shown that NF-κB activation promotes BC migration and invasion [18-21], while TNFα can induce epithelial plasticity and metastatic traits in multiple tumour types [14, 44, 46, 47]. FAM193A therefore appears to set a threshold for inflammatory motility programmes rather than completely preventing NF-κB activation. This is consistent with the modest or variable TNFα responses observed in T24 and BFTC-905 cells, where constitutive pathway activity, lineage state or additional oncogenic alterations may reduce dependence on exogenous TNFα.

In summary, the findings define FAM193A as a stress-responsive suppressor of BC cell motility. Under normal growth conditions, FAM193A is maintained at low abundance by proteasomal degradation, but stabilises following DNA-damage or TNFα stimulation. We provide strong evidence that FAM193A associates with PHD3 and P65. Through stabilisation of PHD3 and modulation of P65-containing complexes, FAM193A limits sustained P65-Ser536 phosphorylation, selected NF-κB transcriptional outputs and TNFα-driven invasion. This model provides a conceptual link between protein-quality control, inflammatory signal termination and urothelial cancer invasion. It also raises the possibility that loss of FAM193A creates a permissive state in which stress and inflammatory cues are converted into prolonged NF-κB activity and enhanced tumour-cell dissemination. Importantly, TNFα/NF-κB-dependent migration and invasion are not restricted to malignant cells but also contribute to physiological processes, including epithelial repair, endothelial regulation, leukocyte transmigration, fibroblast matrix invasion and trophoblast invasion [54-58]. NF-κB can either promote or restrain migration depending on cell type and stimulus, emphasizing that this pathway

functions as a context-dependent regulator rather than a constitutive driver of motility. Similarly, TNFα can promote matrix invasion and trans-endothelial migration in non-malignant human cells, supporting the concept that invasive behaviour per se is not synonymous with malignancy. In BC cells, our data show that FAM193A restrains basal and TNFα-induced migration and invasion by limiting sustained P65/NF-κB activation. FAM193A may therefore regulate the magnitude and duration with which broadly used physiological TNFα/NF-κB motility programmes are engaged. Its loss in cancer could shift these normally transient and tightly controlled responses toward persistent pathological invasion.

Conclusions

FAM193A inhibits the migration and invasion of bladder cancer cells by regulating the PHD3-P65/NF-κB signaling pathway. Under basal conditions, FAM193A is maintained at low levels through proteasome-dependent degradation, but it accumulates during cellular stress responses. Mechanistically, FAM193A binds to PHD3 and P65, promotes PHD3 stability, regulates the assembly of the PHD3-P65 complex, and limits the sustained phosphorylation of P65 at Ser536 and the transcriptional activity of NF-κB. The absence of FAM193A enhances both basal and TNF-α-induced migration and invasion phenotypes, whereas ectopic expression of FAM193A suppresses these responses. In summary, these findings indicate that FAM193A acts as a stress-response regulator in inflammatory signaling pathways and support the model that the FAM193A-PHD3 axis is involved in terminating pro-invasive NF-κB activity in bladder cancer.

Supplementary information

1. Description of Additional Supplementary Files
2. Supplementary Figures S1-S6
3. Supplementary Table ST1
4. Supplementary Table ST2
5. Supplementary Table ST3
6. Supplementary Table ST4
7. Supplementary Table ST5
8. Supplementary Table ST6
9. All WBs with full membrane

Declarations

Ethics approval and consent to participate

Mouse experiments were performed in accordance with the Basel Declaration and have been approved by Baden Württemberg animal ethics committee (approval date: 09.05.2017, approval no. 35/9185.81-3/1326)

Consent for publication

Not applicable

Data availability

The publicly available datasets analysed in this study were obtained from cBioPortal, the UCSC Xena platform, and the Gene Expression Omnibus (GEO; accession numbers GSE48075, GSE32894, and GSE269877). TCGA survival analyses were performed using the Kaplan–Meier Plotter platform. All other data generated or analysed during this study are included in this article and its Supplementary Information files. Uncropped full membranes corresponding to the Western blots presented in the manuscript are provided as a Related

Manuscript File. Additional data are available from the corresponding author upon reasonable request.

Declaration of competing interest

The authors declare no competing interests.

Funding

This study did not receive any specific grant from funding agencies in the public, commercial, or not-for-profit sectors.

Author contributions

C.G. conceived and coordinated the study, analyzed the data, and wrote the manuscript. K.L. performed and analyzed most of the experiments. J.L., X.W. and W.J. performed the shRNA library screening experiments. H.L. generated the HEK293T and SQSTM1 (p62) knockout single-cell clones. X.Z. performed the bioinformatics analyses. Z.W. performed part of the RT–qPCR experiments. G.N. and A.A. contributed to the conception of the study and provided technical guidance throughout the project. C.B. provided financial support. All authors reviewed and approved the final manuscript.

Acknowledgements

We thank Dr. Zdenek Andrysik (Department of Pharmacology, University of Colorado Anschutz Medical Campus, Aurora, CO, USA) for generously providing the Halo-tagged FAM193A full-length and truncation constructs, and Dr. Alexey Ushmorov (Institute of Physiological Chemistry, Ulm University, Ulm, Germany) for kindly providing the 3×κB luciferase reporter plasmid. We also thank Prof. Dr. Thomas Wirth, Dr. Miltiadis Tsesmelis and Dr. Ziwei Du (Institute of Physiological Chemistry, Ulm University, Ulm, Germany) for their valuable suggestions and for generously providing anti-pIKKα/β (Ser176/180) antibody used in this study.

References

1. Siegel RL, Miller KD, Wagle NS, Jemal A. Cancer statistics, 2023. CA Cancer J Clin. 2023;73(1):17-48.

2. Lenis AT, Lec PM, Chamie K, Mshs MD. Bladder Cancer: A Review. JAMA. 2020;324(19):1980-91.

3. Filho AM, Briganti A, Jemal A, Bray F. Bladder Cancer Incidence and Mortality: A Global Overview and Recent Trends. Eur Urol. 2026;89(5):426-36.

4. Patel VG, Oh WK, Galsky MD. Treatment of muscle-invasive and advanced bladder cancer in 2020. CA Cancer J Clin. 2020;70(5):404-23.

5. Cancer Genome Atlas Research N. Comprehensive molecular characterization of urothelial bladder carcinoma. Nature. 2014;507(7492):315-22.

6. Kamoun A, de Reynies A, Allory Y, Sjodahl G, Robertson AG, Seiler R, et al. A Consensus Molecular Classification of Muscle-invasive Bladder Cancer. Eur Urol. 2020;77(4):420-33.

7. Warrick JI, Al-Ahmadie H, Berman DM, Black PC, Flaig TW, Hoglund M, et al. International Society of Urological Pathology Consensus Conference on Current Issues in Bladder Cancer. Working Group 4: Molecular Subtypes of Bladder Cancer-Principles of Classification and Emerging Clinical Utility. Am J Surg Pathol. 2024;48(1):e32-e42.

8. Bruford EA, Braschi B, Denny P, Jones TEM, Seal RL, Tweedie S. Guidelines for human gene nomenclature. Nat Genet. 2020;52(8):754-8.

9. Szwarc MM, Guarnieri AL, Joshi M, Duc HN, Laird MC, Pandey A, et al. FAM193A is a positive regulator of p53 activity. Cell Rep. 2023;42(3):112230.

10. Hayden MS, Ghosh S. Shared principles in NF-kappaB signaling. Cell. 2008;132(3):344-62.

11. Karin M, Greten FR. NF-kappaB: linking inflammation and immunity to cancer development and progression. Nat Rev Immunol. 2005;5(10):749-59.

12. Peng Y, Xiong RP, Wang B, Chen X, Ning YL, Zhao Y, et al. c-Ski is a novel repressor of NF-kappaB through interaction with p65 and HDAC1 in U937 cells. Cell Commun Signal. 2025;23(1):165.

13. Christian F, Smith EL, Carmody RJ. The Regulation of NF-kappaB Subunits by Phosphorylation. Cells. 2016;5(1).

14. Huber MA, Azoitei N, Baumann B, Grunert S, Sommer A, Pehamberger H, et al. NF-kappaB is essential for epithelial-mesenchymal transition and metastasis in a model of breast cancer progression. J Clin Invest. 2004;114(4):569-81.

15. Karin M. Nuclear factor-kappaB in cancer development and progression. Nature. 2006;441(7092):431-6.

16. Oh A, Pardo M, Rodriguez A, Yu C, Nguyen L, Liang O, et al. NF-kappaB signaling in neoplastic transition from epithelial to mesenchymal phenotype. Cell Commun Signal. 2023;21(1):291.

17. Xia Y, Shen S, Verma IM. NF-kappaB, an active player in human cancers. Cancer Immunol Res. 2014;2(9):823-30.

18. Zhu J, Li Y, Chen C, Ma J, Sun W, Tian Z, et al. NF-kappaB p65 Overexpression Promotes Bladder Cancer Cell Migration via FBW7-Mediated Degradation of RhoGDIalpha Protein. Neoplasia. 2017;19(9):672-83.

19. Liu JY, Zeng QH, Cao PG, Xie D, Chen X, Yang F, et al. RIPK4 promotes bladder urothelial carcinoma cell aggressiveness by upregulating VEGF-A through the NF-kappaB pathway. Br J Cancer. 2018;118(12):1617-27.

20. Inoue S, Ide H, Mizushima T, Jiang G, Netto GJ, Gotoh M, et al. Nuclear Factor-kappaB Promotes Urothelial Tumorigenesis and Cancer Progression via Cooperation with Androgen Receptor Signaling. Mol Cancer Ther. 2018;17(6):1303-14.

21. Lee SJ, Cho SC, Lee EJ, Kim S, Lee SB, Lim JH, et al. Interleukin-20 promotes migration of bladder cancer cells through extracellular signal-regulated kinase (ERK)-mediated MMP-9 protein expression leading to nuclear factor (NF-kappaB) activation by inducing the up-regulation of p21(WAF1) protein expression. J Biol Chem. 2013;288(8):5539-52.

22. Epstein AC, Gleadle JM, McNeill LA, Hewitson KS, O'Rourke J, Mole DR, et al. C. elegans EGL-9 and mammalian homologs define a family of dioxygenases that regulate HIF by prolyl hydroxylation. Cell. 2001;107(1):43-54.

23. Fujita N, Gogate SS, Chiba K, Toyama Y, Shapiro IM, Risbud MV. Prolyl hydroxylase 3 (PHD3) modulates catabolic effects of tumor necrosis factor-alpha (TNF-alpha) on cells of the nucleus pulposus through co-activation of nuclear factor kappaB (NF-kappaB)/p65 signaling. J Biol Chem. 2012;287(47):39942-53.

24. Scholz CC, Cavadas MA, Tambuwala MM, Hams E, Rodriguez J, von Kriegsheim A, et al. Regulation of IL-1beta-induced NF-kappaB by hydroxylases links key hypoxic and inflammatory signaling pathways. Proc Natl Acad Sci U S A. 2013;110(46):18490-5.

25. Xue J, Li X, Jiao S, Wei Y, Wu G, Fang J. Prolyl hydroxylase-3 is down-regulated in colorectal cancer cells and inhibits IKKbeta independent of hydroxylase activity. Gastroenterology. 2010;138(2):606-15.

26. Li Y, Yuan T, Zhang H, Liu S, Lun J, Guo J, et al. PHD3 inhibits colon cancer cell metastasis through the occludin-p38 pathway. Acta Biochim Biophys Sin (Shanghai). 2023;55(11):1749-57.

27. Zhou P, Peng X, Tang S, Zhang K, Tan Z, Li D, et al. E3 ligase MAEA-mediated ubiquitination and degradation of PHD3 promotes glioblastoma progression. Oncogene. 2023;42(16):1308-20.

28. Tamura A, Kitayama K, Adachi M, Hashimoto K, Oguro A, Imaoka S. Prolyl hydroxylase domain enzymes (isoforms 1-3, PHD1-3), but not factor-inhibiting HIF-1 (FIH-1), interact with the IKK complex and attenuate LPS-activated NF-kappa-B. J Toxicol Sci. 2025;50(3):105-16.

29. Njeru SN, Kraus J, Meena JK, Lechel A, Katz SF, Kumar M, et al. Aneuploidy-inducing gene knockdowns overlap with cancer mutations and identify Orp3 as a B-cell lymphoma suppressor. Oncogene. 2020;39(7):1445-65.

30. Wezel F, Lustig J, Azoitei A, Liu J, Meessen S, Najjar G, et al. Grainyhead-Like 3 Influences Migration and Invasion of Urothelial Carcinoma Cells. Int J Mol Sci. 2021;22(6).

31. Wang W, Zheng X, Azoitei A, John A, Zengerling F, Wezel F, et al. The Role of TKS5 in Chromosome Stability and Bladder Cancer Progression. Int J Mol Sci. 2022;23(22).

32. Eberhart S, Rother J, Zheng X, Eckstein M, Kriegmair M, Hernandez D, et al. Establishment of Real-Time Multispectral Imaging for the Detection of Bladder Cancer Using a Preclinical in Vivo Model. Bladder Cancer. 2020;6:285-94.

33. Juric I, Fink EE, Qiu H, Desprez PE, Ravi A, Holton M, et al. Single-cell RNA-sequencing of BCG naive and recurrent non-muscle invasive bladder cancer reveals a CD6/ALCAM-mediated immune-suppressive pathway. NPJ Precis Oncol. 2025;9(1):318.

34. Muller-Dott S, Tsirvouli E, Vazquez M, Ramirez Flores RO, Badia IMP, Fallegger R, et al. Expanding the coverage of regulons from high-confidence prior knowledge for accurate estimation of transcription factor activities. Nucleic Acids Res. 2023;51(20):10934-49.

35. Kleinman HK, Jacob K. Invasion assays. Curr Protoc Cell Biol. 2001;Chapter 12:Unit 12 2.

36. Liu J, Jiang W, Wang X, Azoitei A, Liu H, Najjar G, et al. CRISPR and compound screens in a novel ex vivo tissue model identify DDR1 and ETA as regulators of cancer cell invasion. Cell Mol Biol Lett. 2026;31(1).

37. Wang X, Liu J, Azoitei A, Eiseler T, Meessen S, Jiang W, et al. Loss of ORP3 induces aneuploidy and promotes bladder cancer cell invasion through deregulated microtubule and actin dynamics. Cell Mol Life Sci. 2023;80(10):299.

38. Liu J, Wang X, Jiang W, Azoitei A, Eiseler T, Eckstein M, et al. Impairment of alpha-tubulin and F-actin interactions of GJB3 induces aneuploidy in urothelial cells and promotes bladder cancer cell invasion. Cell Mol Biol Lett. 2024;29(1):94.

39. Consortium GT. The GTEx Consortium atlas of genetic regulatory effects across human tissues. Science. 2020;369(6509):1318-30.

40. Vivian J, Rao AA, Nothaft FA, Ketchum C, Armstrong J, Novak A, et al. Toil enables reproducible, open source, big biomedical data analyses. Nat Biotechnol. 2017;35(4):314-6.

41. Choi W, Porten S, Kim S, Willis D, Plimack ER, Hoffman-Censits J, et al. Identification of distinct basal and luminal subtypes of muscle-invasive bladder cancer with different sensitivities to frontline chemotherapy. Cancer Cell. 2014;25(2):152-65.

42. Mathew R, Karp CM, Beaudoin B, Vuong N, Chen G, Chen HY, et al. Autophagy suppresses tumorigenesis through elimination of p62. Cell. 2009;137(6):1062-75.

43. Shen H, Xie Y, Wang Y, Xie Y, Wang Y, Su Z, et al. The ER protein CANX (calnexin)-mediated autophagy protects against alzheimer disease. Autophagy. 2025;21(5):1096-115.

44. Katerinaki E, Evans GS, Lorigan PC, MacNeil S. TNF-alpha increases human melanoma cell invasion and migration in vitro: the role of proteolytic enzymes. Br J Cancer. 2003;89(6):1123-9.

45. Kobelt D, Zhang C, Clayton-Lucey IA, Glauben R, Voss C, Siegmund B, et al. Pro-inflammatory TNF-alpha and IFN-gamma Promote Tumor Growth and Metastasis via Induction of MACC1. Front Immunol. 2020;11:980.

46. Li CW, Xia W, Huo L, Lim SO, Wu Y, Hsu JL, et al. Epithelial-mesenchymal transition induced by TNF-alpha requires NF-kappaB-mediated transcriptional upregulation of Twist1. Cancer Res. 2012;72(5):1290-300.

47. Wolczyk D, Zaremba-Czogalla M, Hryniewicz-Jankowska A, Tabola R, Grabowski K, Sikorski AF, et al. TNF-alpha promotes breast cancer cell migration and enhances the concentration of membrane-associated proteases in lipid rafts. Cell Oncol (Dordr). 2016;39(4):353-63.

48. Sjodahl G, Lauss M, Lovgren K, Chebil G, Gudjonsson S, Veerla S, et al. A molecular taxonomy for urothelial carcinoma. Clin Cancer Res. 2012;18(12):3377-86.

49. Miyake M, Hori S, Morizawa Y, Tatsumi Y, Nakai Y, Anai S, et al. CXCL1-Mediated Interaction of Cancer Cells with Tumor-Associated Macrophages and Cancer-Associated Fibroblasts Promotes Tumor Progression in Human Bladder Cancer. Neoplasia. 2016;18(10):636-46.

50. Sun X, He X, Zhang Y, Hosaka K, Andersson P, Wu J, et al. Inflammatory cell-derived CXCL3 promotes pancreatic cancer metastasis through a novel myofibroblast-hijacked cancer escape mechanism. Gut. 2022;71(1):129-47.

51. Wang N, Liu W, Zheng Y, Wang S, Yang B, Li M, et al. CXCL1 derived from tumor-associated macrophages promotes breast cancer metastasis via activating NF-kappaB/SOX4 signaling. Cell Death Dis. 2018;9(9):880.

52. Bjorkoy G, Lamark T, Brech A, Outzen H, Perander M, Overvatn A, et al. p62/SQSTM1 forms protein aggregates degraded by autophagy and has a protective effect on huntingtin-induced cell death. J Cell Biol. 2005;171(4):603-14.

53. Kageyama S, Gudmundsson SR, Sou YS, Ichimura Y, Tamura N, Kazuno S, et al. p62/SQSTM1-droplet serves as a platform for autophagosome formation and anti-oxidative stress response. Nat Commun. 2021;12(1):16.

54. Chiu WC, Chiou TJ, Chiang AN. beta(2)-Glycoprotein I inhibits endothelial cell migration through the nuclear factor kappaB signalling pathway and endothelial nitric oxide synthase activation. Biochem J. 2012;445(1):125-33.

55. de Jong AL, Green DM, Trial JA, Birdsall HH. Focal effects of mononuclear leukocyte transendothelial migration: TNF-alpha production by migrating monocytes promotes subsequent migration of lymphocytes. J Leukoc Biol. 1996;60(1):129-36.

56. Schirren CG, Scharffetter K, Hein R, Braun-Falco O, Krieg T. Tumor necrosis factor alpha induces invasiveness of human skin fibroblasts in vitro. J Invest Dermatol. 1990;94(5):706-10.

57. White SR, Fischer BM, Marroquin BA, Stern R. Interleukin-1beta mediates human airway epithelial cell migration via NF-kappaB. Am J Physiol Lung Cell Mol Physiol. 2008;295(6):L1018-27.

58. Yagel S, Parhar RS, Jeffrey JJ, Lala PK. Normal nonmetastatic human trophoblast cells share in vitro invasive properties of malignant cells. J Cell Physiol. 1988;136(3):455-62.

Figure 1. *FAM193A* is downregulated in invasive BC and predicts poor patient outcome

A. Schematic of the pooled shRNA screening strategy. RT4 cells infected with a pooled shRNA library were subjected to iterative Boyden chamber invasion selection. Invaded cells were collected after 2 days, expanded, re-seeded into new Boyden chambers for two additional rounds of enrichment. Genomic DNA was subsequently isolated, followed by PCR amplification and sequencing to identify enriched shRNAs. Candidate genes were prioritized through subsequent expression and clinical analyses.

B. Relative *FAM193A* mRNA expression measured by qPCR in bladder cell lines grouped according to invasive potential, including HBLAK and Y235T (immortalized urothelial cells), BC61 and RT4 (low-invasive), RT112 and TCC-SUP (medium-invasive), T24, UMUC-3, and BFTC-905 (high-invasive). Group means were compared with the high-invasive group using one-way ANOVA followed by multiple-comparisons testing. Data are presented as mean ± SEM from three independent experiments (except for TCC-SUP, n = 2 independent experiments).

C. Frequency of *FAM193A* genomic alterations across human cancer types obtained from cBioPortal.

D. *FAM193A* expression in normal bladder tissues and primary bladder tumours from the combined TCGA-BLCA and GTEx cohorts using a two-sided Wilcoxon rank-sum test. RNA-seq data were obtained from the UCSC Toil recompute dataset integrating TCGA-BLCA and GTEx samples and analysed in-house using R.

E. *FAM193A* expression in non-muscle-invasive BC (NMIBC) and muscle-invasive BC (MIBC) samples from the GSE48075 cohort. Statistical significance was determined using a two-sided Wilcoxon rank-sum test.

F. Kaplan–Meier analysis of overall survival in the TCGA BC cohort (n = 404) performed using the KM Plotter platform using a two-sided log-rank test.

G. Kaplan–Meier analysis of overall survival in the GSE48075 cohort using a two-sided log-rank test.

H. Kaplan–Meier analysis of disease-specific survival in the GSE48075 cohort using a two-sided log-rank test.

P values are indicated in the panels. *P < 0.05, **P < 0.01, ***P < 0.001, and ****P < 0.0001.

Figure 2. *FAM193A* inhibits the invasion and migration capabilities of BC cells.

A. Relative *FAM193A* mRNA expression in RT4 cells following knockdown with three independent shRNAs and in T24 and BFTC-905 cells following ectopic expression of *FAM193A*. FAM193A overexpression was validated at both the mRNA and protein levels using a V5-tagged construct. Mean ± SEM, n = 3 independent experiments; one-way ANOVA or two-sided Student's t-test, as appropriate.

B. Matrigel-coated Boyden chamber invasion assays in RT4 (6 days), T24 (2 days), and BFTC-905 (2 days) cells. Representative images are shown, and invasion was quantified by counting cells on the lower surface of the membrane. Mean ± SEM, n = 4 independent experiments; one-way ANOVA or two-sided Student's t-test, as appropriate.

C. Wound-healing assays in RT4, T24, and BFTC-905 cells, with representative images and time-course quantification of cell-free areas. Wound areas at each time point were normalized to the corresponding area at 0 h, which was set to 1. Mean ± SEM, n = 3 independent experiments; two-way ANOVA (column factor).

D. Schematic of the CRISPR–Cas9-mediated knockout strategy and clonal selection workflow. Two independent knockout clones were validated by genomic DNA Sanger sequencing and ICE (Inference of CRISPR Edits) analysis.

E. Representative images of the ex vivo porcine bladder invasion assay using RT4-p53DD gGFP control clones (top) and FAM193A-knockout clones (bottom), generated using two independent GFP- or FAM193A-targeting gRNAs, respectively. Cells were cultured on porcine bladder tissue for 28 days. Human cells were identified using a human-specific anti-mitochondrial antibody (MAB1273).

F. Quantification of RT4-p53DD cell invasion depth, measured from the seeding surface to the 30 deepest invading cells within the bladder tissue. Mean ± SEM, n = 3 independent experiments; one-way ANOVA followed by multiple-comparisons testing.

G. Representative images of the ex vivo porcine bladder invasion assay using T24 cells stably expressing EV (left) or FAM193A-V5 (right) after 14 days on porcine bladder tissue. Human cells were identified using a human-specific anti-HLA antibody.

H. Quantification of T24 cell invasion depth using the same method described in F. Mean ± SEM, n = 3 independent experiments; Student's t-test.

For **E** and **G**, the culture medium was replaced every second day. Red arrows indicate representative invading cells; green arrows indicate non-invading cells.

I. Hanging-drop aggregation assays in RT4-p53DD control and FAM193A-knockout clones, and T24/BFTC-905 EV and FAM193A-overexpressing cells. The experiment was independently repeated three times with similar results.

Figure 3. FAM193A is constitutively degraded under normal growth conditions but becomes stabilized following DNA damage.

A. HEK293T cells were transfected with FAM193A-V5 and subjected to blasticidin selection for the indicated time-points. Cells were collected at the indicated time points during selection.

B. HEK293T cells stably expressing FAM193A-V5 were treated with MG132 (5 μM), MG132 plus actinomycin D (ActD, 2 μg ml^{-1}), or doxorubicin (Dox, 1 μM) as indicated.

C. T24 and BFTC-905 cells stably expressing FAM193A-V5 were treated with MG132 (5 μM) plus actinomycin D (ActD, 2 μg ml^{-1}) for the indicated times.

D. T24 and BFTC-905 cells stably expressing FAM193A-V5 were treated with doxorubicin (Dox, 1 μM) for the indicated times.

For A–**D**, FAM193A-V5 protein and mRNA levels were analysed by immunoblotting (**Top panels**) and RT–qPCR (**Bottom panels**), respectively. RT–qPCR data are presented as mean ± SEM from three independent experiments, except for the EV group in **A** (n = 2).

E. Subcellular fractionation of HEK293T cells transiently expressing FAM193A-V5 under different extraction conditions, followed by immunoblotting. Calnexin, VDAC1/3, Lamin A/C and α-tubulin were used as compartment-specific markers.

F. Representative immunofluorescence images of FAM193A-V5 localization in HEK293T cells. Golgi apparatus, endoplasmic reticulum, mitochondria, nuclear envelope, LC3 and F-actin were visualized using the indicated markers. The experiment was performed once.

G. Representative immunofluorescence images of HEK293T cells transiently transfected with FAM193A-V5 under normal growth conditions or following doxorubicin treatment (Dox, 1 μM, 24 h). Diffuse, reticular and aggresome-like FAM193A-V5 staining patterns were quantified from the representative experiment shown. The experiment was independently repeated three times with similar results.

H. Representative immunofluorescence images of FAM193A-V5 and p62 colocalization in HEK293T and HeLa cells under normal growth conditions or after doxorubicin treatment (Dox, 1 μM, 24 h). Fluorescence intensity profiles generated using ZEN software illustrate their spatial colocalization.

I. Reciprocal co-immunoprecipitation of FAM193A-V5 and endogenous p62 in HEK293T cells under normal growth conditions or following doxorubicin (Dox, 1 μM, 24 h), hypoxia (1% O_2, 20 h), or H_2O_2 (1 mM, 1 h) treatment. IgG served as a negative control and endogenous MDM4 as a positive control for FAM193A binding. Input lysates are shown below.

J. Control and p62-knockout HEK293T cells stably expressing empty vector (EV) or FAM193A-V5 were treated with doxorubicin (Dox, 1 μM, 24 h), as indicated. Protein levels of FAM193A-V5, p62, phospho-p62 (Ser349) and LC3 were analysed by immunoblotting.

Figure 4. FAM193A interacts with PHD3 and promotes PHD3 stability during cellular stress.

A. Immunoblot analysis of canonical NF-κB signalling components in HEK293T cells stably expressing FAM193A-V5 followed by CRISPR-mediated depletion of FAM193A using the indicated sgRNAs. Phosphorylation of P65 (Ser536), IκBα (Ser32), and IKKα/β (Ser176/180), together with total P65, was analysed by immunoblotting.

B. BioGRID interaction-network Venn diagram generated using Venny, identifying PHD3 (EGLN3) as the only overlap among FAM193A, p62 (SQSTM1), P65 (RELA) and IκBα (NFKBIA) networks.

C. Representative proximity ligation assay (PLA) images showing the interaction between FAM193A-V5 and endogenous PHD3 in HEK293T cells transiently transfected with empty vector (EV) or FAM193A-V5. Nuclei were counterstained with DAPI. The experiment was performed once.

D. PHD3 immunoblotting in HEK293T cells expressing control or FAM193A-targeting sgRNAs, untreated or treated with Dox (1 μM, 24 h). GAPDH loading control.

E. PHD3 immunoblotting in pooled RT4-p53DD control and FAM193A-knockout cells, untreated or treated with Dox (1 μM, 24 h). GAPDH loading control.

F. PHD3 immunoblotting in RT4-p53DD control and FAM193A-knockout single-cell clones under basal conditions or after MG132 (5 μM, 4 h), Dox (1 μM, 24 h), hypoxia (1% O_2, 20 h) or H_2O_2 (1 mM, 1 h). GAPDH or α-tubulin loading controls, as indicated.

G. Co-IP in HEK293T cells transiently expressing FAM193A-V5, untreated or treated with doxorubicin (Dox, 1 μM, 24 h). V5 IP assessed FAM193A binding to P65 and MDM4 (positive control); reciprocal PHD3 IP assessed endogenous PHD3 association with FAM193A and P65.

FAM193A–PHD3 binding was quantified relative to untreated FAM193A-V5 (= 1) per experiment. Mean ± SEM, n = 4 independent experiments; two-tailed unpaired Student's t-test.

H. Results from sequential IP experiments with HEK293T cells stably expressing EV (HEK293T-EV) or PHD3 (HEK293T-PHD3) cells that were transiently transfected with EV or FAM193A-V5. PHD3 IP was followed by non-denaturing elution and P65 re-IP.

Figure 5. FAM193A regulates dynamic interactions between PHD3 and P65 during TNFα-induced NF-κB signalling

A. Co-IP analysis of FAM193A, PHD3 and P65 interactions in HEK293T cells transiently transfected with empty vector (EV) or FAM193A-V5 following TNFα stimulation (10 ng mL^{-1}) for the indicated times. V5, PHD3 or P65 antibodies were used for immunoprecipitation, as indicated. Quantification and data analysis of FAM193A–P65, FAM193A–PHD3 and PHD3–P65 interactions is shown in Fig. S5A.

B. Co-immunoprecipitation analysis of HEK293T cells stably overexpressing PHD3 and transiently transfected with EV or FAM193A-V5 following TNFα stimulation (10 ng mL^{-1}) for the indicated times. PHD3 was immunoprecipitated, and co-immunoprecipitated FAM193A-V5, P65, and phospho-P65 (Ser536) were analysed by immunoblotting. Input lysates are shown below.

C. Representative proximity ligation assay (PLA) images showing the interaction between FAM193A-V5 and endogenous P65 in HEK293T cells transiently transfected with FAM193A-V5 following TNFα stimulation (10 ng mL^{-1}) for the indicated times. Nuclei were counterstained with DAPI (n=2 independent experiments).

D. Representative PLA images showing the interaction between FAM193A-V5 and endogenous PHD3 in HEK293T cells transiently transfected with FAM193A-V5 following TNFα stimulation (10 ng mL^{-1}) for the indicated times. Nuclei were counterstained with DAPI. (n=2 independent experiments).

E. Representative PLA images showing the interaction between endogenous PHD3 and endogenous P65 in parental HEK293T cells following TNFα stimulation (10 ng mL^{-1}) for the indicated times. Nuclei were counterstained with DAPI. Similar TNFα-dependent changes in PHD3–P65 PLA signals were independently observed in two additional experiments using

HEK293T cells stably expressing EV or PHD3 and HEK293T cells expressing shScr or shPHD3.

F. Nuclear–cytoplasmic fractionation of HEK293T cells stably expressing EV or PHD3 following TNFα stimulation (10 ng mL^{-1}) for the indicated times. Cytoplasmic (CE) and nuclear (NE) fractions were analysed by immunoblotting for phospho-P65 (Ser536), total P65, and P50. PHD3 expression is shown at low and high exposures. GAPDH and stain-free total protein served as loading controls for the cytoplasmic and nuclear fractions, respectively.

Figure 6. FAM193A impairs sustained NF-κB activation

A. (**Left**) Results of immunoblot analyses of TNFα-induced NF-κB signalling in HEK293T cells stably expressing empty vector (EV) or FAM193A-V5. Cells were stimulated with TNFα (10 ng mL^{-1}) for the indicated times. (**Right**) Phospho-P65 (Ser536) levels were normalized to total P65 and quantified relative to EV containing cells at 15 min (= 1). Mean ± SEM, n = 3 independent experiments; two-way ANOVA with multiple-comparisons testing.

B. (**Left**) Results of immunoblot analyses of TNFα-induced (10 ng mL^{-1}) P65 phosphorylation in HEK293T-FAM193A-V5 cells following CRISPR-mediated re-targeting of FAM193A using two independent gRNAs. EV + gGFP cells served as an additional control. Phospho-P65 (Ser536) was normalized to total P65 and quantified relative to FAM193A-V5 + gGFP at 0 min (= 1). Mean ± SEM, n = 3 independent experiments; two-way ANOVA with multiple-comparisons testing.

C. (**Left**) Results of immunoblot analyses of TNFα-induced (10 ng mL^{-1}) NF-κB signalling in RT4-p53DD cells with gGFP control and gFAM193A knockout clones for the indicated times. Representative blots from one control and one knockout clone are shown. (**Right**) Quantification included two independent clones per genotype in each of three independent experiments. Phospho-P65 (Ser536) was normalized to total P65 and expressed relative to

the corresponding knockout condition at 1 h (= 1). Mean ± SEM, n = 3 independent experiments; two-way ANOVA with multiple-comparisons test.

D. (**Left**) Results of immunoblot analyses of TNFα-induced (10 ng mL^{-1}) NF-κB signalling in BFTC-905 cells stably expressing EV or FAM193A-V5 for the indicated times. (**Right**) Phospho-P65 (Ser536) was normalized to total P65 and quantified relative to EV at 30 min (= 1). Mean ± SEM, n = 3 independent experiments; two-way ANOVA with multiple-comparisons testing.

E. (**Middle**) Results of immunoblot analyses of TNFα-induced (10 ng mL^{-1}) NF-κB signalling in T24 cells stably expressing EV or FAM193A-V5 for the indicated times. (**Right**) Phospho-P65 (Ser536) was normalized to total P65 and quantified relative to EV at 30 min (= 1). Mean ± SEM, n = 3 independent experiments; two-way ANOVA with multiple-comparisons testing.

F. Results of immunoblot analyses of TNFα-induced NF-κB signalling in HEK293T cells stably expressing EV or FAM193A-V5, followed by control shRNA (shScr) or shPHD3-2. Cells were stimulated with TNFα (10 ng mL^{-1}) for the indicated times. Similar results were observed in three independent experiments.

G. NF-κB reporter activity in HEK293T cells transiently expressing EV or FAM193A-V5 following treatment with TNFα (10 ng mL^{-1}, 6 h), doxorubicin (Dox, 1 μM, 24 h), hypoxia (1% O_2, 20 h), or H_2O_2 (1 mM, 4 h), as indicated. Firefly/Renilla activity was quantified relative to untreated EV containing cells (= 1). Mean ± SEM, n = 3 independent experiments; one-way ANOVA with multiple-comparisons test.

H. NF-κB reporter activity in HEK293T cells transiently expressing the indicated combinations of EV, FAM193A, and PHD3 following TNFα stimulation (10 ng mL^{-1}, 6 h). Firefly/Renilla activity was quantified relative to untreated EV containing cells (= 1). Mean ± SEM, n = 3 independent experiments; one-way ANOVA with multiple-comparisons test.

I. (**Top**) Schematic of Halo-tagged full-length FAM193A (FL) and the indicated truncation mutants. (**Bottom**) NF-κB reporter activity was measured in HEK293T cells expressing the indicated constructs following TNFα stimulation (10 ng mL^{-1}, 24 h). Firefly/Renilla activity was quantified relative to untreated EV containing cells (= 1). Mean ± SEM, n = 3 independent experiments; one-way ANOVA with multiple-comparisons test.

J. Halo pull-down analysis of endogenous P65 and PHD3 associated with the indicated Halo-tagged FAM193A fragments in HEK293T-Parental cells transiently transfected with the indicated Halo constructs. Whole-cell lysates (Input) are shown below. The position of the full-length (FL) Halo-FAM193A protein at low exposure is indicated by an arrow.

K. Halo pull-down analysis of endogenous P65 and PHD3 associated with the indicated Halo-tagged FAM193A fragments in HEK293T-PHD3OE cells transiently expressing the indicated Halo-tagged FAM193A constructs. Whole-cell lysates (Input) are shown below. The position of the full-length (FL) Halo-FAM193A protein at low exposure is indicated by an arrow.

Figure 7. FAM193A limits TNFα-driven invasive and migratory responses downstream of NF-κB.

A. Representative Boyden chamber images of RT4 cells treated with TNFα (0, 5, 10, 20, 40, or 60 ng mL^{-1}) for six days, with medium containing TNFα replaced every 48 h. Five fields of view were analysed per condition. The experiment was performed once.

B. Quantification of invading RT4 cells shown in A. Data represent technical replicates from one independent experiment.

C. RT4 cell viability following TNFα treatment at the indicated concentrations for six days, measured by MTT assay. Mean ± SEM, n = 3 independent experiments.

D. Validation of P65 knockdown in RT4 cells expressing two independent P65 shRNAs by RT-qPCR of *RELA*. Mean ± SEM, n = 3 independent experiments; one-way ANOVA with multiple-comparisons test.

E. Boyden chamber invasion assay of RT4 control (shScr) and P65-knockdown cells treated with or without TNFα (10 ng mL^{-1}) for six days. Fresh medium with or without TNFα was added to the lower chamber and replaced every 48 h. Quantification of invading cells is shown on the left, and representative images are shown on the right. Mean ± SEM, n = 4 independent experiments; two-way ANOVA with multiple-comparisons test.

F. Immunoblot validation of P65 knockdown in RT4 control and P65-knockdown cells following long-term TNFα treatment (10 ng mL^{-1}). Fresh medium containing TNFα was replenished every 48 h.

G. Representative Boyden chamber images of RT4-p53DD gGFP control and FAM193A-knockout cells treated with or without TNFα (5 ng mL^{-1}) for six days. Fresh medium with or without TNFα was added to the lower chamber and replaced every 48 h. Two independent gGFP control clones and two independent FAM193A-knockout clones are shown.

H. Quantification of invading RT4-p53DD gGFP control and FAM193A-knockout cells shown in **G**. Mean ± SEM, n = 4 independent experiments; two-way ANOVA with multiple-comparisons test.

I. Representative wound-healing images of RT4-p53DD gGFP control and FAM193A-knockout cells cultured in the absence or presence of TNFα (5 ng mL^{-1}) for 24 h.

J. Quantification of wound closure shown in I. Cell-free areas at 24 h were normalized to the corresponding cell-free area at 0 h, which was set to 1. Mean ± SEM, n = 4 independent experiments; two-way ANOVA with multiple-comparisons test.

K. Correlation matrix showing the association between *FAM193A* expression and the expression of selected NF-κB pathway-related genes in the GSE32894 BC cohort. Circle size indicates −log10(*P*), and colour represents the Pearson correlation coefficient.

L. Patient-level Spearman correlations between FAM193A and the six NF-κB-related genes across 23 independent urothelial pseudo-bulk profiles. Spearman rho values and Benjamini–Hochberg-adjusted FDR values are indicated.

M. Standardized *FAM193A* coefficients from linear models adjusted for BCG-naïve versus recurrent sample status across the 23 independent patient-level profiles. Points indicate estimated standardized coefficients and horizontal lines indicate 95% confidence intervals; the dashed line denotes β = 0.

N. Association between *FAM193A* expression and the selected six-gene *RELA*-positive target score across 23 independent patient-level profiles (rho = −0.66, P < 0.001).

O. Association between *FAM193A* expression and the broader *RELA*-positive target score (rho = −0.36, P = 0.091). In N and O, solid lines indicate linear fits with 95% confidence bands for visualization, whereas the reported statistics are based on Spearman correlation.

P. Permutation analysis testing the specificity of the six-gene *RELA*-positive target score. Ten thousand random six-gene sets were sampled from the remaining *RELA*-positive target genes, scored using the same procedure as the observed six-gene set, and correlated with *FAM193A*. The observed correlation (rho = −0.66) fell within the extreme negative tail of the null distribution (median rho = −0.136; one-sided empirical P = 0.0039).

Q. RT-qPCR analysis of selected NF-κB-responsive genes in RT4-p53DD gGFP control and FAM193A-knockout cells treated with or without TNFα (5 ng mL^{-1}) for 8 hours. Relative mRNA expression levels are shown. Mean ± SEM, n = 3 independent experiments; two-way ANOVA with multiple-comparisons test.

Figure S1. Validation of the Boyden chamber screening strategy and reduced *Fam193a* expression in a murine BC model.

A. Schematic illustration of the Boyden chamber invasion assay. During the first 8 days, RT4 cells remained within the Matrigel layer, whereas invasive cells became detectable at the bottom of the well after prolonged incubation (>10 days).

B. Representative bright-field images of RT4 parental cells detected at the bottom of the well in the Boyden chamber invasion assay at the indicated time points. RT4 parental cells were barely detectable at the bottom of the well during the first 8 days, whereas invasive cells became visible after prolonged incubation from day 10 onwards. Black circles highlight representative invaded cells.

C. Representative bright-field images of cells detected at the bottom of the well following knockdown of *GJB3* or *ORP3* in RT4 cells. *GJB3* and *ORP3* were previously identified as suppressors of BC cell invasion and therefore served as positive controls for the Boyden chamber screening strategy. Red arrows indicate invaded cells.

D. Relative *Fam193a* mRNA expression in bladder tissues from control mice (n = 21) and BBN-induced bladder tumours (n = 19), measured by qPCR. Data are presented as mean ± SEM. Statistical significance was determined using a two-sided unpaired Welch's t-test. $P < 0.05$.

Figure S2. Validation of *FAM193A* genetic knockout and its effect on cell growth.

A. Cell viability measured by MTT assays in RT4 cells expressing control shRNA (shLuc) or three independent FAM193A-targeting shRNAs, and in T24 and BFTC-905 cells stably expressing EV or FAM193A-V5. Data are presented as mean ± SEM from three independent experiments for RT4 and T24 cells and four independent experiments for BFTC-905 cells. Statistical significance was determined using two-way ANOVA followed by multiple-comparisons testing.

B. Validation of FAM193A knockout clones generated by CRISPR/Cas9-mediated genome editing in RT4-p53DD cells by Sanger sequencing and ICE (Inference of CRISPR Edits) analysis. Representative sequencing chromatograms and ICE analysis are shown for the gGFP control clone and two independent FAM193A knockout clones. Both knockout clones contain frameshift-inducing insertions or deletions at the gRNA target site, resulting in altered reading frames and premature stop codons.

C. *Ex vivo* porcine bladder invasion assay with BFTC-905 cells stably expressing EV or FAM193A-V5. Cells were cultured on porcine bladder tissue for 14 days and the culture medium replaced every second day. Representative immunohistochemical staining images are shown. Human cells (BFTC-905 and derivatives) were identified using a human-specific anti-mitochondrial antibody (MAB1273). Green arrows indicate non-invading cells. No detectable invasion into the underlying bladder tissue was observed in either group during the 14-day observation period. The experiment was independently repeated three times with similar results.

Figure S3. FAM193A is constitutively degraded under normal growth conditions but becomes stabilized following DNA damage.

A. Immunoblot analysis of V5-tagged FAM193A expression in HEK293T cells following prolonged blasticidin selection for the indicated durations. α-Tubulin was used as a loading control.

B. Immunoprecipitation of V5-tagged FAM193A expressed in HEK293T cells. Immunoprecipitated proteins were analysed by immunoblotting using antibodies against V5, total ubiquitin, K48-linked ubiquitin, and K63-linked ubiquitin, as indicated. Input lysates are shown on the left. The experiment was performed once.

C. Immunoblot analysis of V5-tagged FAM193A expression in T24 and BFTC-905 cells treated with MG132 (5 μM) for the indicated times. GAPDH or β-actin was used as a loading control.

D. Immunoblot analysis of V5-tagged FAM193A expression in BFTC-905 cells following treatment with EGF (10 ng mL^{-1}) or H_2O_2 (100 μM) for the indicated times. β-Actin was used as a loading control. The experiment was performed once.

Figure S4. FAM193A selectively regulates the PHD3–NF-κB axis.

A. Immunoblot analysis of EGF-induced signalling in T24 cells stably expressing empty vector (EV) or FAM193A-V5 following EGF stimulation for the indicated times. Phosphorylation of ERK, AKT, STAT3 and FAK, together with H-Ras, was analysed by immunoblotting. β-Actin was used as a loading control. The experiment was performed once.

B. Immunoblot analysis of EGF-induced signalling in BFTC-905 cells stably expressing empty vector (EV) or FAM193A-V5 following EGF stimulation for the indicated times. Phosphorylation of ERK and AKT, together with c-Jun, H-Ras, R-Ras and FAK, was analysed by immunoblotting. β-Actin was used as a loading control. The experiment was performed once.

C. Immunoblot analysis of proteins associated with cell adhesion, cytoskeletal organization and signalling pathways in T24 cells stably expressing empty vector (EV) or FAM193A-V5. Expression of VE-cadherin, P21, FAK, phospho-STAT3 (Tyr705), phospho-YAP (Ser127), Cdc42, phospho-Cofilin (Ser3), EB1 and GSK3β was analysed. GAPDH was used as a loading control. The experiment was performed once.

D. Immunoblot analysis of NF-κB signalling components in T24 and BFTC-905 cells stably expressing empty vector (EV) or FAM193A-V5. Expression of FAM193A-V5, phospho-P65 (Ser536), total P65, phospho-p62 (Ser349) and total p62 was analysed by immunoblotting. The experiment was performed once.

E. Co-immunoprecipitation analysis of HEK293T-PHD3-OE cells transiently transfected with FAM193A-V5 under the indicated conditions (hypoxia, 1% O_2 for 20 h; H_2O_2, 1 mM for 1 h). FAM193A-V5 was immunoprecipitated using a V5 antibody, and co-precipitated PHD3 was detected by immunoblotting. This experiment was performed once as a complementary analysis to the co-immunoprecipitation of endogenous PHD3.

Figure S5. Additional analyses of FAM193A–PHD3–P65 complex dynamics during TNFα signalling

A. Quantification of FAM193A–P65, FAM193A–PHD3 and PHD3–P65 interactions shown in Fig. 5A following TNFα stimulation (10 ng mL^{-1}) for the indicated times. FAM193A–P65 and FAM193A–PHD3 interaction levels were normalized within each independent experiment to the corresponding 0-min condition, which was set to 100%. PHD3–P65 interaction levels were normalized within each independent experiment to the EV 0-min condition, which was set to 100%. Mean ± SEM, n = 3 independent experiments for FAM193A–P65 and n = 4 independent experiments for FAM193A–PHD3 and PHD3–P65; one-way ANOVA with multiple-comparisons test.

B. Extended time-course co-immunoprecipitation analysis of FAM193A, PHD3 and P65 interactions in HEK293T cells transiently transfected with empty vector (EV) or FAM193A-V5 following TNFα stimulation (10 ng mL^{-1}) for the indicated times. V5, PHD3 or P65 antibodies were used for immunoprecipitation, as indicated. Whole-cell lysates (Input) are shown below. The experiment was performed once.

C. Validation of PHD3 knockdown and overexpression in HEK293T cells expressing control shRNA (shScr), two independent PHD3-targeting shRNAs (shPHD3-1 and shPHD3-2), or ectopically expressed PHD3, as indicated. PHD3 protein expression was analysed by immunoblotting, with GAPDH used as a loading control. The immunoblotting experiment was performed once. PHD3 mRNA expression was analysed by qPCR. qPCR data: Mean ± SEM, n = 3 independent experiments.

D. Co-immunoprecipitation analysis using a P65 antibody in HEK293T cells expressing control shRNA (shScr) or shPHD3-2 and transiently transfected with empty vector (EV) or FAM193A-V5 following TNFα stimulation (10 ng mL^{-1}) for the indicated times. Co-immunoprecipitated FAM193A-V5 and IκBα were analysed by immunoblotting. Whole-cell lysates (Input) are shown below. The experiment was performed once.

E. Representative proximity ligation assay (PLA) images showing endogenous PHD3–P65 interactions in HEK293T cells expressing control shRNA (shScr) or shPHD3-2 following TNFα stimulation (10 ng mL^{-1}) for the indicated times. Nuclei were counterstained with DAPI. The experiment was performed once.

F. Quantification of TNFα-induced (10 ng mL^{-1}) nuclear translocation of P65 (left) and P50 (right) in HEK293T cells stably expressing empty vector (EV) or PHD3. Nuclear P65 and P50 levels were normalized for nuclear protein loading and expressed relative to the EV 0-min condition within each independent experiment, which was set to 100%. Mean ± SEM, n = 3 independent experiments; two-way ANOVA with multiple-comparisons test.

Figure S6. FAM193A regulates BC cell migration and NF-κB-responsive gene expression.

A. Representative Boyden chamber invasion images of T24 cells stably expressing empty vector (EV) or FAM193A-V5 treated with or without TNFα (10 ng mL^{-1}). Cells were cultured for one day, and fresh medium containing TNFα was added at the time of seeding.

B. Quantification of invading T24 cells shown in A. Mean ± SEM, n = 4 independent experiments; two-way ANOVA with multiple-comparisons test.

C. Representative wound-healing images of T24 cells stably expressing empty vector (EV) or FAM193A-V5 cultured in the absence or presence of TNFα (10 ng mL^{-1}) for 12 h.

D. Quantification of wound closure shown in C. Cell-free areas at 12 h were normalized to the corresponding cell-free area at 0 h, which was set to 1. Mean ± SEM, n = 3 independent experiments; two-way ANOVA with multiple-comparisons test.

E. Representative Boyden chamber invasion images of BFTC-905 cells stably expressing empty vector (EV) or FAM193A-V5 treated with or without TNFα (10 ng mL^{-1}). Cells were cultured for 48 h, with TNFα-containing medium added at the time of seeding.

F. Quantification of the invasion area of BFTC-905 cells shown in E. Invasion area is expressed as a percentage of the total field area. Mean ± SEM, n = 4 independent experiments; two-way ANOVA with multiple-comparisons test.

G. Representative wound-healing images of BFTC-905 cells stably expressing empty vector (EV) or FAM193A-V5 cultured in the absence or presence of TNFα (10 ng mL^{-1}) for 12 h.

H. Quantification of wound closure shown in G. Cell-free areas at 12 h were normalized to the corresponding cell-free area at 0 h, which was set to 1. Mean ± SEM, n = 4 independent experiments; two-way ANOVA with multiple-comparisons test.

I. Cell viability of T24 and BFTC-905 cells treated with the indicated concentrations of TNFα for 2 days, measured by MTT assay. Mean ± SEM, n = 3 independent experiments.

J. RT-qPCR analysis of selected NF-κB-responsive genes in T24 cells stably expressing empty vector (EV) or FAM193A-V5 treated with or without TNFα (10 ng mL^{-1}) for 8 hours. Relative mRNA expression levels are shown. Mean ± SEM, n = 3 independent experiments; two-way ANOVA with multiple-comparisons test.

K. RT-qPCR analysis of selected NF-κB-responsive genes in BFTC-905 cells stably expressing empty vector (EV) or FAM193A-V5 treated with or without TNFα (10 ng mL^{-1}) for 8 h. Relative mRNA expression levels are shown. Mean ± SEM, n = 3 independent experiments; two-way ANOVA with multiple-comparisons test.

L. Immunoblot analyses of PHD3 expression in RT4 cells expressing control (shScr) or PHD3-targeting shRNA. The accompanying immunoblotting analysis was performed once. Representative Boyden chamber invasion images and quantification of these cells after 6 days are shown. Mean ± SEM, n = 4 independent experiments; Student's t-test. The accompanying immunoblotting analysis was performed once.

M. Immunoblot analysis of PHD3 expression in T24 cells stably expressing empty vector (EV) or PHD3. The accompanying immunoblotting analysis was performed once. Representative Boyden chamber invasion images and quantification of these cells after 1 day are shown. Mean ± SEM, n = 4 independent experiments; Student's t-test.

N. Immunoblot analysis of FAM193A-V5 and PHD3 expression in BFTC-905 stable cell pools expressing empty vector (EV), FAM193A-V5, PHD3, or both FAM193A-V5 and PHD3. Representative Boyden chamber invasion images and quantification of these cells treated with or without TNFα (20 ng mL^{-1}) for 2 days are shown. Mean ± SEM, n = 3 independent experiments; two-way ANOVA with multiple-comparisons test.

O. Immunoblot analysis of FAM193A-V5 and PHD3 expression in two independent EV control clones (EV #3 and #4) and two FAM193A/PHD3 double-overexpression clones (#1 and #13) derived from BFTC-905 cells. Representative Boyden chamber invasion images and quantification following treatment with or without TNFα (20 ng mL^{-1}) for 2 days are shown. Data from the two clones within each group were combined for statistical analysis. Mean ± SEM, n = 3 independent experiments; two-way ANOVA with multiple-comparisons test.

Figures

Figure 1

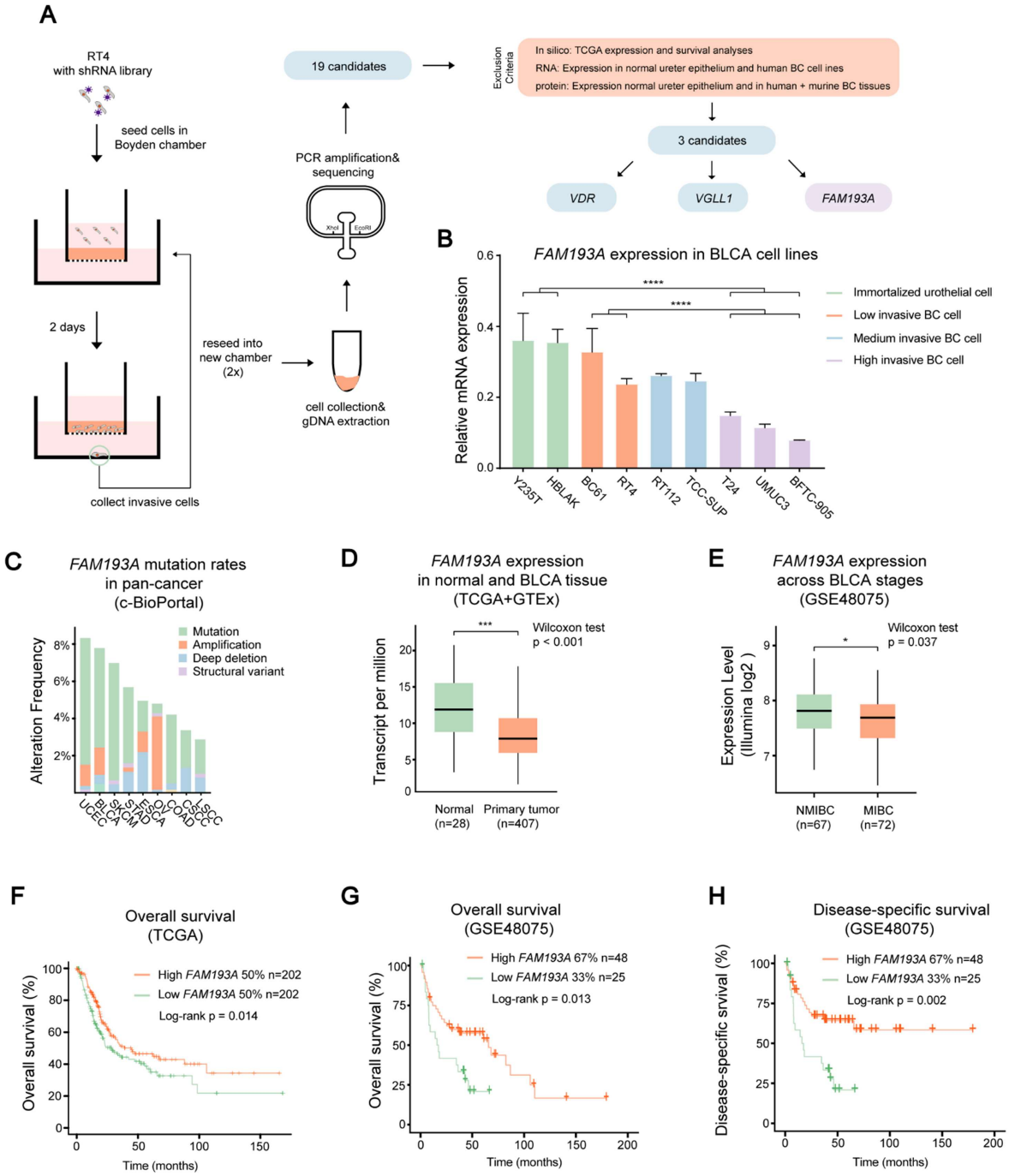


Figure 0

***FAM193A* is downregulated in invasive BC and predicts poor patient outcome**

A. Schematic of the pooled shRNA screening strategy. RT4 cells infected with a pooled shRNA library were subjected to iterative Boyden chamber invasion selection. Invaded cells were collected after 2 days, expanded, re-seeded into new Boyden chambers for two additional rounds of enrichment. Genomic DNA was subsequently isolated, followed by PCR amplification and sequencing to identify enriched shRNAs. Candidate genes were prioritized through subsequent expression and clinical analyses.

B. Relative *FAM193A* mRNA expression measured by qPCR in bladder cell lines grouped according to invasive potential, including HBLAK and Y235T (immortalized urothelial cells), BC61 and RT4 (low-invasive), RT112 and TCC-SUP (medium-invasive), T24, UMUC-3, and BFTC-905 (high-invasive). Group means were compared with the high-invasive group using one-way ANOVA followed by multiple-comparisons testing. Data are presented as mean ± SEM from three independent experiments (except for TCC-SUP, n = 2 independent experiments).

C. Frequency of *FAM193A* genomic alterations across human cancer types obtained from cBioPortal.

D. *FAM193A* expression in normal bladder tissues and primary bladder tumours from the combined TCGA-BLCA and GTEx cohorts using a two-sided Wilcoxon rank-sum test. RNA-seq data were obtained from the UCSC Toil recompute dataset integrating TCGA-BLCA and GTEx samples and analysed in-house using R.

E. *FAM193A* expression in non-muscle-invasive BC (NMIBC) and muscle-invasive BC (MIBC) samples from the GSE48075 cohort. Statistical significance was determined using a two-sided Wilcoxon rank-sum test.

F. Kaplan–Meier analysis of overall survival in the TCGA BC cohort (n = 404) performed using the KM Plotter platform using a two-sided log-rank test.

G. Kaplan–Meier analysis of overall survival in the GSE48075 cohort using a two-sided log-rank test.

H. Kaplan–Meier analysis of disease-specific survival in the GSE48075 cohort using a two-sided log-rank test.

P values are indicated in the panels. *P < 0.05, **P < 0.01, ***P < 0.001, and ****P < 0.0001.

Figure 2

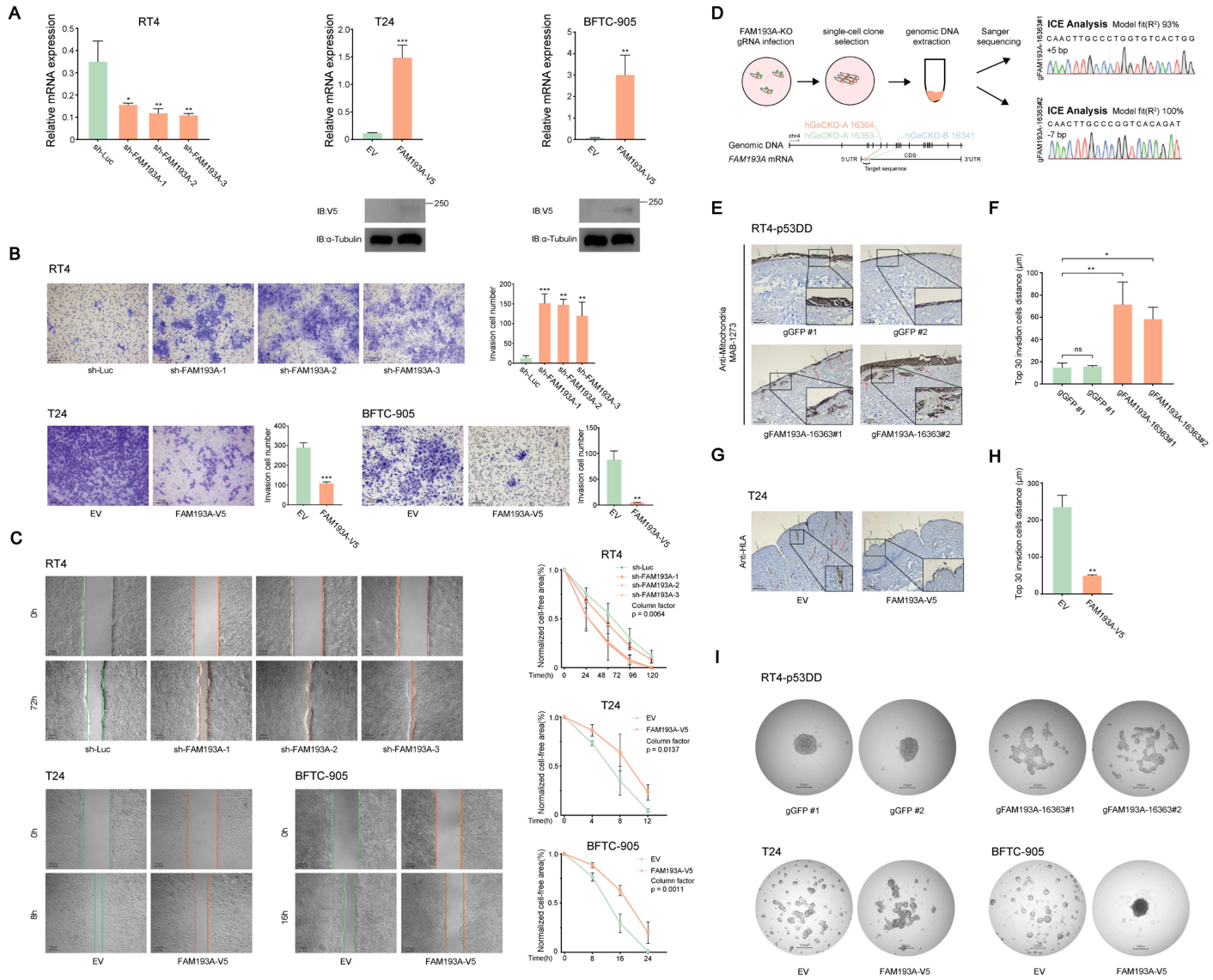


Figure 1

***FAM193A*inhibits the invasion and migration capabilities of BC cells.**

A.Relative *FAM193A* mRNA expression in RT4 cells following knockdown with three independent shRNAs and in T24 and BFTC-905 cells following ectopic expression of *FAM193A*. FAM193A overexpression was validated at both the mRNA and protein levels using a V5-tagged construct. Mean ± SEM, n = 3 independent experiments; one-way ANOVA or two-sided Student's t-test, as appropriate.

B. Matrigel-coated Boyden chamber invasion assays in RT4 (6 days), T24 (2 days), and BFTC-905 (2 days) cells. Representative images are shown, and invasion was quantified by counting cells on the lower surface of the membrane. Mean ± SEM, n = 4 independent experiments; one-way ANOVA or two-sided Student's t-test, as appropriate.

C.Wound-healing assays in RT4, T24, and BFTC-905 cells, with representative images and time-course quantification of cell-free areas. Wound areas at each time point were normalized to the corresponding area at 0 h, which was set to 1. Mean ± SEM, n = 3 independent experiments; two-way ANOVA (column factor).

D.Schematic of the CRISPR–Cas9-mediated knockout strategy and clonal selection workflow. Two independent knockout clones were validated by genomic DNA Sanger sequencing and ICE (Inference of CRISPR Edits) analysis.

E. Representative images of the ex vivo porcine bladder invasion assay using RT4-p53DD gGFP control clones (top) and FAM193A-knockout clones (bottom), generated using two independent GFP- or FAM193A-targeting gRNAs, respectively. Cells were cultured on porcine bladder tissue for 28 days. Human cells were identified using a human-specific anti-mitochondrial antibody (MAB1273).

F. Quantification of RT4-p53DD cell invasion depth, measured from the seeding surface to the 30 deepest invading cells within the bladder tissue. Mean ± SEM, n = 3 independent experiments; one-way ANOVA followed by multiple-comparisons testing.

G. Representative images of the ex vivo porcine bladder invasion assay using T24 cells stably expressing EV (left) or FAM193A-V5 (right) after 14 days on porcine bladder tissue. Human cells were identified using a human-specific anti-HLA antibody.

H. Quantification of T24 cell invasion depth using the same method described in F. Mean ± SEM, n = 3 independent experiments; Student’s t-test.

For **E** and **G**, the culture medium was replaced every second day. Red arrows indicate representative invading cells; green arrows indicate non-invading cells.

I. Hanging-drop aggregation assays in RT4-p53DD control and FAM193A-knockout clones, and T24/BFTC-905 EV and FAM193A-overexpressing cells. The experiment was independently repeated three times with similar results.

Figure 3

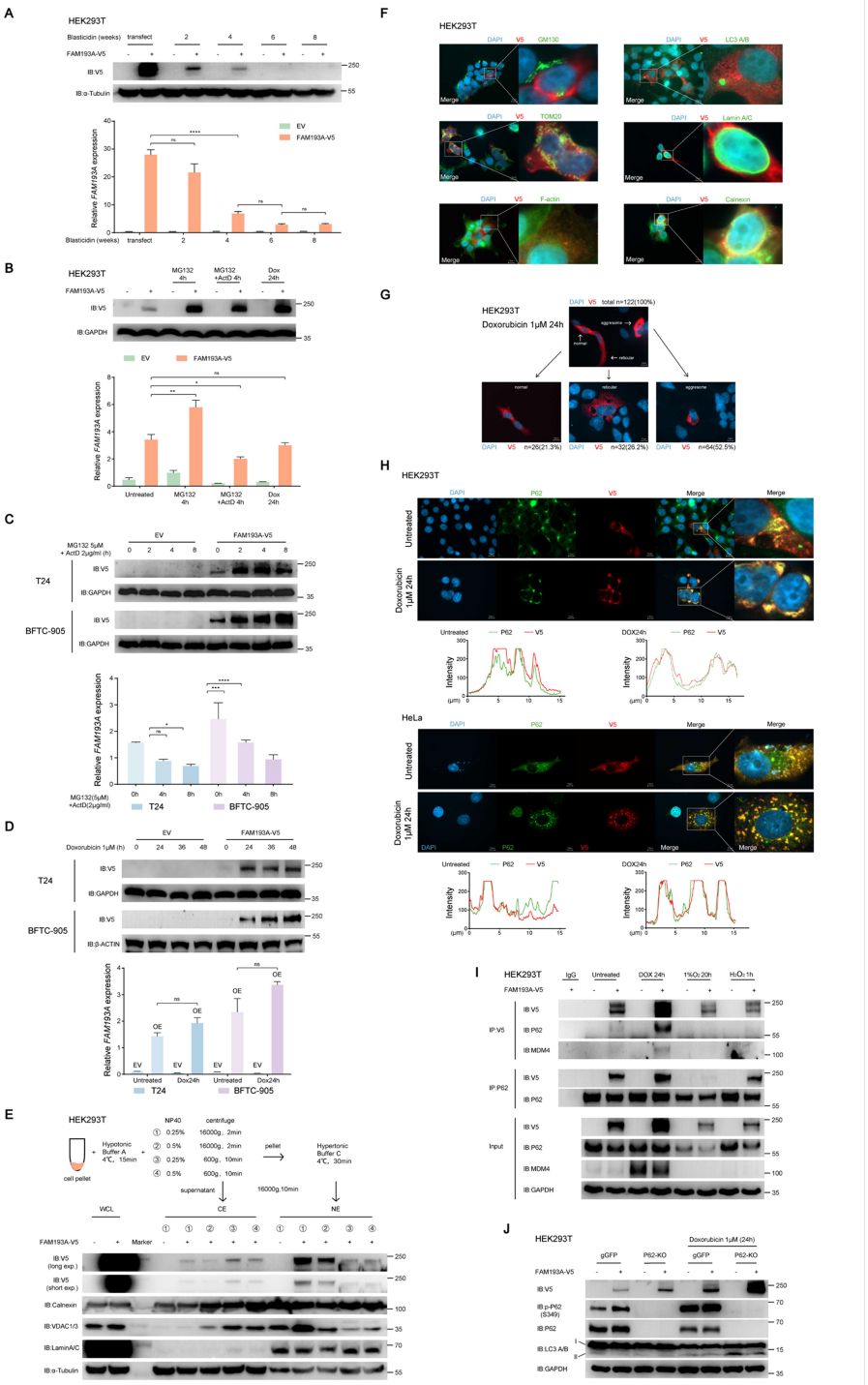


Figure 2

FAM193A is constitutively degraded under normal growth conditions but becomes stabilized following DNA damage.

A.HEK293T cells were transfected with FAM193A-V5 and subjected to blasticidin selection for the indicated time-points. Cells were collected at the indicated time points during selection.

B.HEK293T cells stably expressing FAM193A-V5 were treated with MG132 (5 μM), MG132 plus actinomycin D (ActD, 2 μg ml^{-1}), or doxorubicin (Dox, 1 μM) as indicated.

C.T24 and BFTC-905 cells stably expressing FAM193A-V5 were treated with MG132 (5 μM) plus actinomycin D (ActD, 2 μg ml^{-1}) for the indicated times.

D.T24 and BFTC-905 cells stably expressing FAM193A-V5 were treated with doxorubicin (Dox, 1 μM) for the indicated times.

For A–**D**, FAM193A-V5 protein and mRNA levels were analysed by immunoblotting (**Top panels**) and RT–qPCR (**Bottom panels**), respectively. RT–qPCR data are presented as mean ± SEM from three independent experiments, except for the EV group in **A**(n = 2).

E. Subcellular fractionation of HEK293T cells transiently expressing FAM193A-V5 under different extraction conditions, followed by immunoblotting. Calnexin, VDAC1/3, Lamin A/C and α-tubulin were used as compartment-specific markers.

F.Representative immunofluorescence images of FAM193A-V5 localization in HEK293T cells. Golgi apparatus, endoplasmic reticulum, mitochondria, nuclear envelope, LC3 and F-actin were visualized using the indicated markers. The experiment was performed once.

G. Representative immunofluorescence images of HEK293T cells transiently transfected with FAM193A-V5 under normal growth conditions or following doxorubicin treatment (Dox, 1 μM, 24 h). Diffuse, reticular and aggresome-like FAM193A-V5 staining patterns were quantified from the representative experiment shown. The experiment was independently repeated three times with similar results.

H. Representative immunofluorescence images of FAM193A-V5 and p62 colocalization in HEK293T and HeLa cells under normal growth conditions or after doxorubicin treatment (Dox, 1 μM, 24 h). Fluorescence intensity profiles generated using ZEN software illustrate their spatial colocalization.

I.Reciprocal co-immunoprecipitation of FAM193A-V5 and endogenous p62 in HEK293T cells under normal growth conditions or following doxorubicin (Dox, 1 μM, 24 h), hypoxia (1% O_2, 20 h), or H_2O_2(1 mM, 1 h) treatment. IgG served as a negative control and endogenous MDM4 as a positive control for FAM193A binding. Input lysates are shown below.

J.Control and p62-knockout HEK293T cells stably expressing empty vector (EV) or FAM193A-V5 were treated with doxorubicin (Dox, 1 μM, 24 h), as indicated. Protein levels of FAM193A-V5, p62, phospho-p62 (Ser349) and LC3 were analysed by immunoblotting.

Figure 4

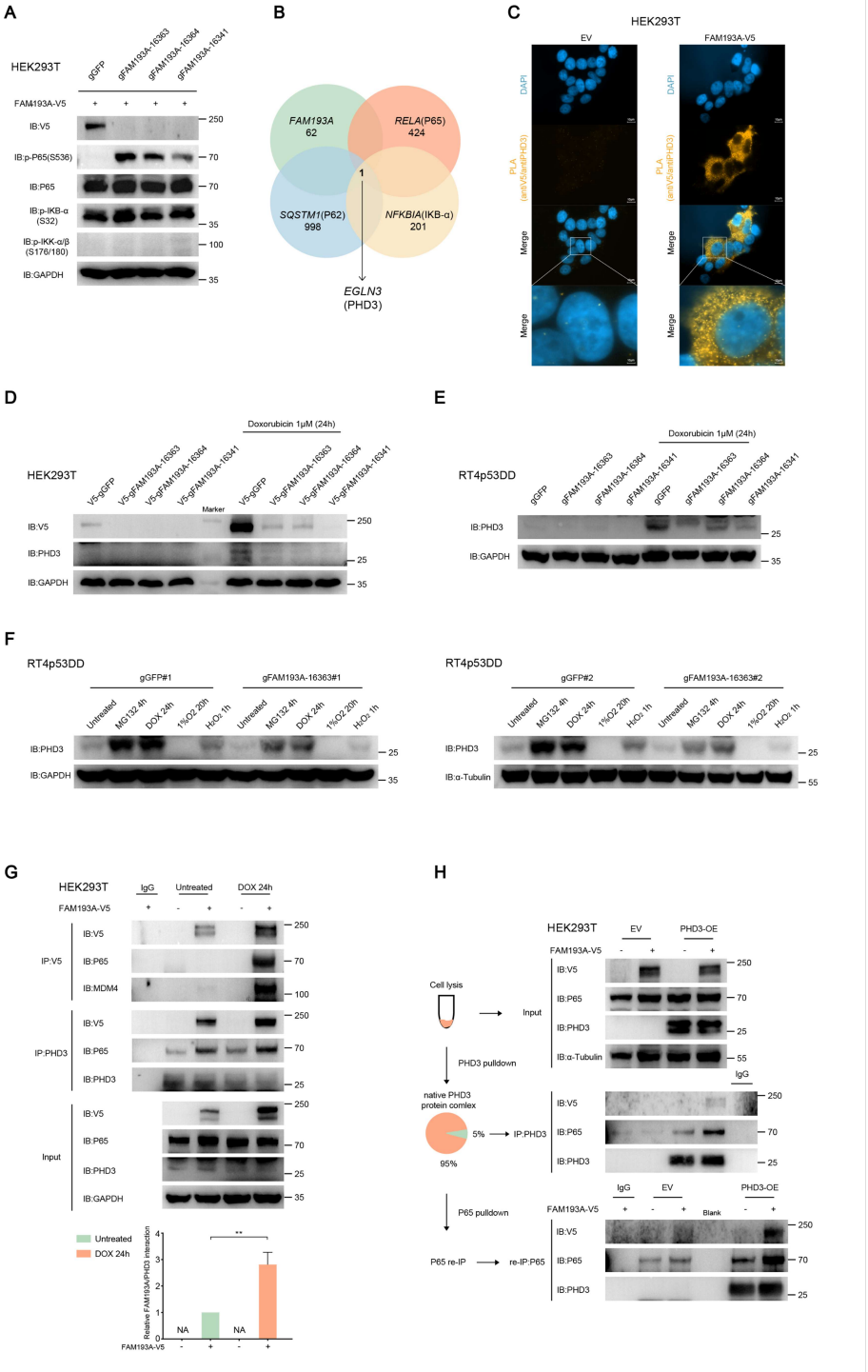


Figure 3

FAM193A interacts with PHD3 and promotes PHD3 stability during cellular stress.

A.Immunoblot analysis of canonical NF-κB signalling components in HEK293T cells stably expressing FAM193A-V5 followed by CRISPR-mediated depletion of FAM193A using the indicated sgRNAs.

Phosphorylation of P65 (Ser536), IκBα (Ser32), and IKKα/β (Ser176/180), together with total P65, was analysed by immunoblotting.

B. BioGRID interaction-network Venn diagram generated using Venny, identifying PHD3 (EGLN3) as the only overlap among FAM193A, p62 (SQSTM1), P65 (RELA) and IκBα (NFKBIA) networks.

C.Representative proximity ligation assay (PLA) images showing the interaction between FAM193A-V5 and endogenous PHD3 in HEK293T cells transiently transfected with empty vector (EV) or FAM193A-V5. Nuclei were counterstained with DAPI. The experiment was performed once.

D. PHD3 immunoblotting in HEK293T cells expressing control or FAM193A-targeting sgRNAs, untreated or treated with Dox (1 μM, 24 h). GAPDH loading control.

E. PHD3 immunoblotting in pooled RT4-p53DD control and FAM193A-knockout cells, untreated or treated with Dox (1 μM, 24 h). GAPDH loading control.

F. PHD3 immunoblotting in RT4-p53DD control and FAM193A-knockout single-cell clones under basal conditions or after MG132 (5 μM, 4 h), Dox (1 μM, 24 h), hypoxia (1% O_2, 20 h) or H_2O_2(1 mM, 1 h). GAPDH or α-tubulin loading controls, as indicated.

G.Co-IP in HEK293T cells transiently expressing FAM193A-V5, untreated or treated with doxorubicin (Dox, 1 μM, 24 h). V5 IP assessed FAM193A binding to P65 and MDM4 (positive control); reciprocal PHD3 IP assessed endogenous PHD3 association with FAM193A and P65. FAM193A–PHD3 binding was quantified relative to untreated FAM193A-V5 (= 1) per experiment. Mean ± SEM, n = 4 independent experiments; two-tailed unpaired Student's t-test.

H.Results from sequential IP experiments with HEK293T cells stably expressing EV (HEK293T-EV) or PHD3 (HEK293T-PHD3) cells that were transiently transfected with EV or FAM193A-V5. PHD3 IP was followed by non-denaturing elution and P65 re-IP.

Figure 5

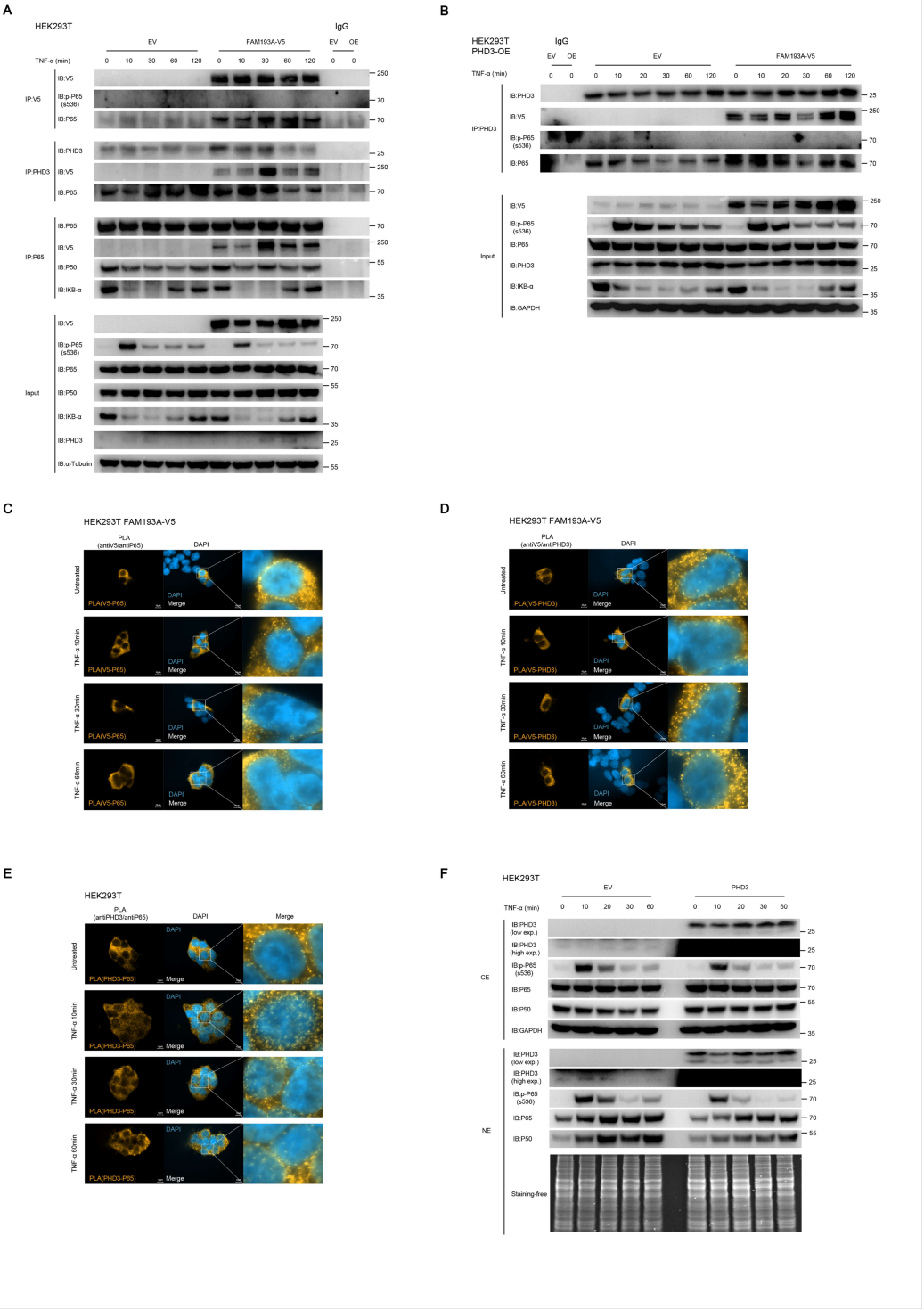


Figure 4

FAM193A regulates dynamic interactions between PHD3 and P65 during TNFα-induced NF-κB signalling

A. Co-IP analysis of FAM193A, PHD3 and P65 interactions in HEK293T cells transiently transfected with empty vector (EV) or FAM193A-V5 following TNFα stimulation (10 ng mL^{-1}) for the indicated times. V5,

PHD3 or P65 antibodies were used for immunoprecipitation, as indicated. Quantification and data analysis of FAM193A–P65, FAM193A–PHD3 and PHD3–P65 interactions is shown in Fig. S5A.

B. Co-immunoprecipitation analysis of HEK293T cells stably overexpressing PHD3 and transiently transfected with EV or FAM193A-V5 following TNFα stimulation (10 ng mL^{-1}) for the indicated times. PHD3 was immunoprecipitated, and co-immunoprecipitated FAM193A-V5, P65, and phospho-P65 (Ser536) were analysed by immunoblotting. Input lysates are shown below.

C. Representative proximity ligation assay (PLA) images showing the interaction between FAM193A-V5 and endogenous P65 in HEK293T cells transiently transfected with FAM193A-V5 following TNFα stimulation (10 ng mL^{-1}) for the indicated times. Nuclei were counterstained with DAPI (n=2 independent experiments).

D. Representative PLA images showing the interaction between FAM193A-V5 and endogenous PHD3 in HEK293T cells transiently transfected with FAM193A-V5 following TNFα stimulation (10 ng mL^{-1}) for the indicated times. Nuclei were counterstained with DAPI. (n=2 independent experiments).

E. Representative PLA images showing the interaction between endogenous PHD3 and endogenous P65 in parental HEK293T cells following TNFα stimulation (10 ng mL^{-1}) for the indicated times. Nuclei were counterstained with DAPI. Similar TNFα-dependent changes in PHD3–P65 PLA signals were independently observed in two additional experiments using HEK293T cells stably expressing EV or PHD3 and HEK293T cells expressing shScr or shPHD3.

F. Nuclear–cytoplasmic fractionation of HEK293T cells stably expressing EV or PHD3 following TNFα stimulation (10 ng mL^{-1}) for the indicated times. Cytoplasmic (CE) and nuclear (NE) fractions were analysed by immunoblotting for phospho-P65 (Ser536), total P65, and P50. PHD3 expression is shown at low and high exposures. GAPDH and stain-free total protein served as loading controls for the cytoplasmic and nuclear fractions, respectively.

Figure 6

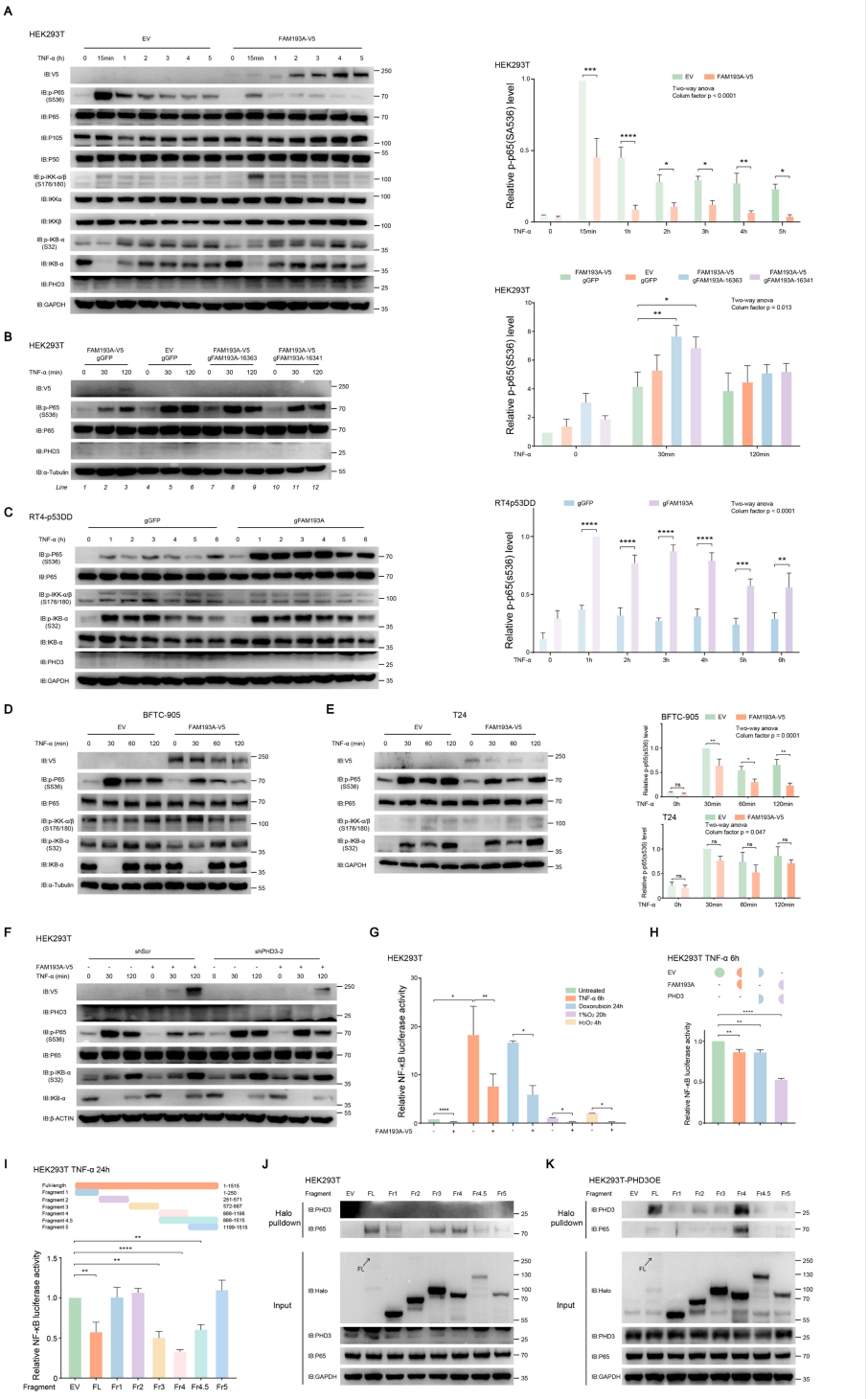


Figure 5

FAM193A impairs sustained NF-κB activation

A. (**Left**) Results of immunoblot analyses of TNFα-induced NF-κB signalling in HEK293T cells stably expressing empty vector (EV) or FAM193A-V5. Cells were stimulated with TNFα (10 ng mL⁻¹) for the indicated times. (**Right**) Phospho-P65 (Ser536) levels were normalized to total P65 and quantified

relative to EV containing cells at 15 min (= 1). Mean ± SEM, n = 3 independent experiments; two-way ANOVA with multiple-comparisons testing.

B. (**Left**) Results of immunoblot analyses of TNFα-induced (10 ng mL^{-1}) P65 phosphorylation in HEK293T-FAM193A-V5 cells following CRISPR-mediated re-targeting of FAM193A using two independent gRNAs. EV + gGFP cells served as an additional control. Phospho-P65 (Ser536) was normalized to total P65 and quantified relative to FAM193A-V5 + gGFP at 0 min (= 1). Mean ± SEM, n = 3 independent experiments; two-way ANOVA with multiple-comparisons testing.

C. (**Left**) Results of immunoblot analyses of TNFα-induced (10 ng mL^{-1}) NF-κB signalling in RT4-p53DD cells with gGFP control and gFAM193A knockout clones for the indicated times. Representative blots from one control and one knockout clone are shown. (**Right**) Quantification included two independent clones per genotype in each of three independent experiments. Phospho-P65 (Ser536) was normalized to total P65 and expressed relative to the corresponding knockout condition at 1 h (= 1). Mean ± SEM, n = 3 independent experiments; two-way ANOVA with multiple-comparisons test.

D. (**Left**) Results of immunoblot analyses of TNFα-induced (10 ng mL^{-1}) NF-κB signalling in BFTC-905 cells stably expressing EV or FAM193A-V5 for the indicated times. (**Right**) Phospho-P65 (Ser536) was normalized to total P65 and quantified relative to EV at 30 min (= 1). Mean ± SEM, n = 3 independent experiments; two-way ANOVA with multiple-comparisons testing.

E. (**Middle**) Results of immunoblot analyses of TNFα-induced (10 ng mL^{-1}) NF-κB signalling in T24 cells stably expressing EV or FAM193A-V5 for the indicated times. (**Right**) Phospho-P65 (Ser536) was normalized to total P65 and quantified relative to EV at 30 min (= 1). Mean ± SEM, n = 3 independent experiments; two-way ANOVA with multiple-comparisons testing.

F. Results of immunoblot analyses of TNFα-induced NF-κB signalling in HEK293T cells stably expressing EV or FAM193A-V5, followed by control shRNA (shScr) or shPHD3-2. Cells were stimulated with TNFα (10 ng mL^{-1}) for the indicated times. Similar results were observed in three independent experiments.

G. NF-κB reporter activity in HEK293T cells transiently expressing EV or FAM193A-V5 following treatment with TNFα (10 ng mL^{-1}, 6 h), doxorubicin (Dox, 1 μM, 24 h), hypoxia (1% O_2, 20 h), or H_2O_2 (1 mM, 4 h), as indicated. Firefly/Renilla activity was quantified relative to untreated EV containing cells (= 1). Mean ± SEM, n = 3 independent experiments; one-way ANOVA with multiple-comparisons test.

H. NF-κB reporter activity in HEK293T cells transiently expressing the indicated combinations of EV, FAM193A, and PHD3 following TNFα stimulation (10 ng mL^{-1}, 6 h). Firefly/Renilla activity was quantified relative to untreated EV containing cells (= 1). Mean ± SEM, n = 3 independent experiments; one-way ANOVA with multiple-comparisons test.

I. (**Top**) Schematic of Halo-tagged full-length FAM193A (FL) and the indicated truncation mutants. (**Bottom**) NF-κB reporter activity was measured in HEK293T cells expressing the indicated constructs following TNFα stimulation (10 ng mL^{-1}, 24 h). Firefly/Renilla activity was quantified relative to untreated

EV containing cells (= 1). Mean ± SEM, n = 3 independent experiments; one-way ANOVA with multiple-comparisons test.

J. Halo pull-down analysis of endogenous P65 and PHD3 associated with the indicated Halo-tagged FAM193A fragments in HEK293T-Parental cells transiently transfected with the indicated Halo constructs. Whole-cell lysates (Input) are shown below. The position of the full-length (FL) Halo-FAM193A protein at low exposure is indicated by an arrow.

K. Halo pull-down analysis of endogenous P65 and PHD3 associated with the indicated Halo-tagged FAM193A fragments in HEK293T-PHD3OE cells transiently expressing the indicated Halo-tagged FAM193A constructs. Whole-cell lysates (Input) are shown below. The position of the full-length (FL) Halo-FAM193A protein at low exposure is indicated by an arrow.

Figure 7

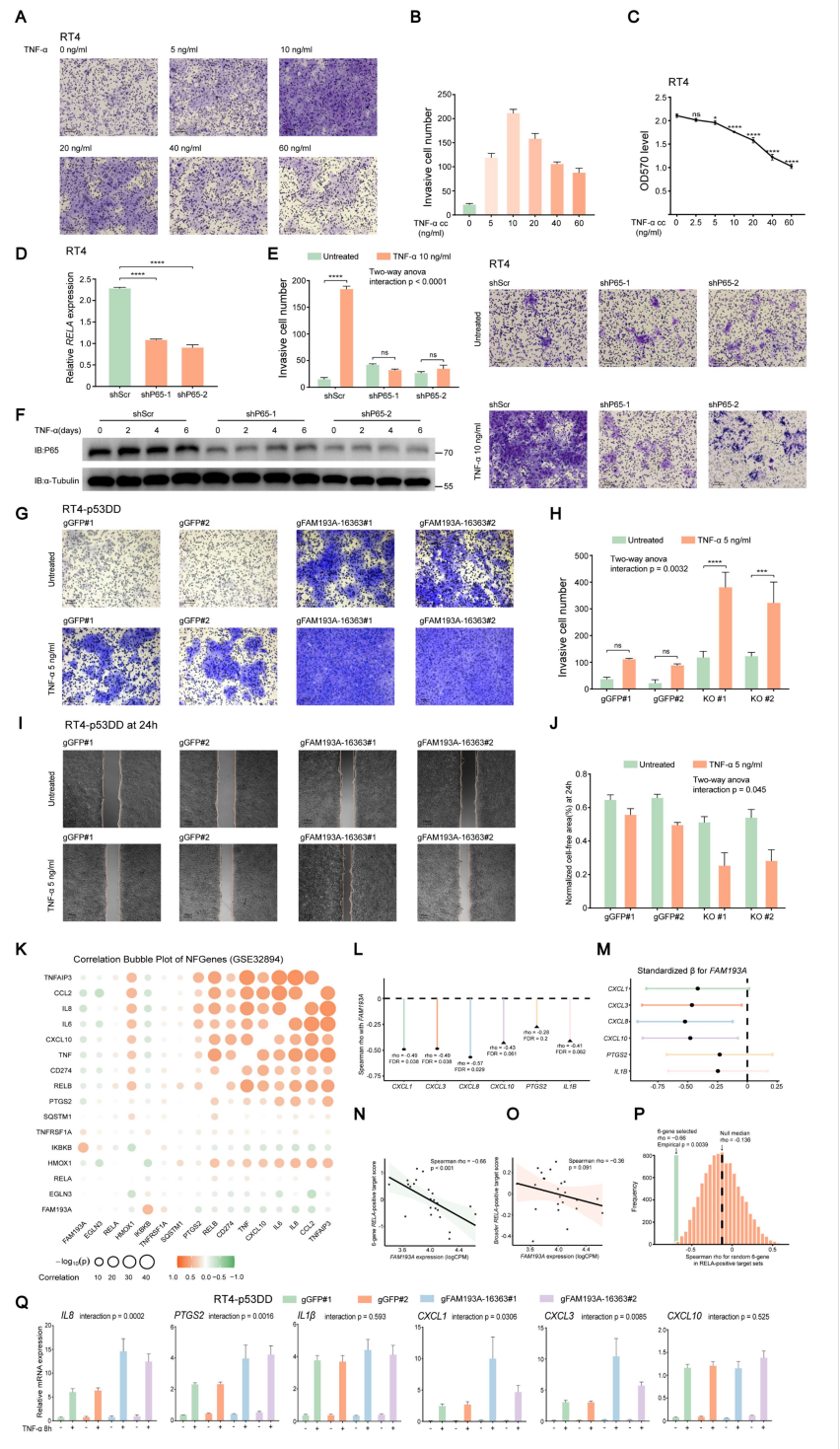


Figure 6

FAM193A limits TNFα-driven invasive and migratory responses downstream of NF-κB.

A.Representative Boyden chamber images of RT4 cells treated with TNFα (0, 5, 10, 20, 40, or 60 ng mL⁻¹) for six days, with medium containing TNFα replaced every 48 h. Five fields of view were analysed per condition. The experiment was performed once.

B.Quantification of invading RT4 cells shown in A. Data represent technical replicates from one independent experiment.

C.RT4 cell viability following TNFα treatment at the indicated concentrations for six days, measured by MTT assay. Mean ± SEM, n = 3 independent experiments.

D.Validation of P65 knockdown in RT4 cells expressing two independent P65 shRNAs by RT-qPCR of *RELA*. Mean ± SEM, n = 3 independent experiments; one-way ANOVA with multiple-comparisons test.

E. Boyden chamber invasion assay of RT4 control (shScr) and P65-knockdown cells treated with or without TNFα (10 ng mL⁻¹) for six days. Fresh medium with or without TNFα was added to the lower chamber and replaced every 48 h. Quantification of invading cells is shown on the left, and representative images are shown on the right. Mean ± SEM, n = 4 independent experiments; two-way ANOVA with multiple-comparisons test.

F.Immunoblot validation of P65 knockdown in RT4 control and P65-knockdown cells following long-term TNFα treatment (10 ng mL⁻¹). Fresh medium containing TNFα was replenished every 48 h.

G. Representative Boyden chamber images of RT4-p53DD gGFP control and FAM193A-knockout cells treated with or without TNFα (5 ng mL⁻¹) for six days. Fresh medium with or without TNFα was added to the lower chamber and replaced every 48 h. Two independent gGFP control clones and two independent FAM193A-knockout clones are shown.

H.Quantification of invading RT4-p53DD gGFP control and FAM193A-knockout cells shown in **G**. Mean ± SEM, n = 4 independent experiments; two-way ANOVA with multiple-comparisons test.

I.Representative wound-healing images of RT4-p53DD gGFP control and FAM193A-knockout cells cultured in the absence or presence of TNFα (5 ng mL⁻¹) for 24 h.

J. Quantification of wound closure shown in I. Cell-free areas at 24 h were normalized to the corresponding cell-free area at 0 h, which was set to 1. Mean ± SEM, n = 4 independent experiments; two-way ANOVA with multiple-comparisons test.

K.Correlation matrix showing the association between *FAM193A* expression and the expression of selected NF-κB pathway-related genes in the GSE32894 BC cohort. Circle size indicates −log10(*P*), and colour represents the Pearson correlation coefficient.

L.Patient-level Spearman correlations between FAM193A and the six NF-κB-related genes across 23 independent urothelial pseudo-bulk profiles. Spearman rho values and Benjamini–Hochberg-adjusted FDR values are indicated.

M.Standardized *FAM193A* coefficients from linear models adjusted for BCG-naïve versus recurrent sample status across the 23 independent patient-level profiles. Points indicate estimated standardized coefficients and horizontal lines indicate 95% confidence intervals; the dashed line denotes β = 0.

N.Association between *FAM193A*expression and the selected six-gene *RELA*-positive target score across 23 independent patient-level profiles (rho = −0.66, P < 0.001).

O.Association between *FAM193A*expression and the broader *RELA*-positive target score (rho = −0.36, P = 0.091). In N and O, solid lines indicate linear fits with 95% confidence bands for visualization, whereas the reported statistics are based on Spearman correlation.

P.Permutation analysis testing the specificity of the six-gene *RELA*-positive target score. Ten thousand random six-gene sets were sampled from the remaining *RELA*-positive target genes, scored using the same procedure as the observed six-gene set, and correlated with *FAM193A*. The observed correlation (rho = −0.66) fell within the extreme negative tail of the null distribution (median rho = −0.136; one-sided empirical P = 0.0039).

Q.RT-qPCR analysis of selected NF-κB-responsive genes in RT4-p53DD gGFP control and FAM193A-knockout cells treated with or without TNFα (5 ng mL^{-1}) for 8 hours. Relative mRNA expression levels are shown. Mean ± SEM, n = 3 independent experiments; two-way ANOVA with multiple-comparisons test.

Supplementary Files

This is a list of supplementary files associated with this preprint. Click to download.

- figureS1.tif
- figureS2.tif
- figureS3.tif
- figureS4.tif
- figureS5.tif
- figureS6.tif
- SupplementaryFilesDescription.xlsx
- SupplementaryTableST1.xlsx
- SupplementaryTableST3.xlsx
- SupplementaryTableST4.xlsx
- SupplementaryTableST2.xlsx
- SupplementaryTableST5.xlsx
- SupplementaryTableST6.xlsx
- AllWBswithuncroppedfullmembranes.pdf
- Supply.docx